# Ice state evolution during spring in Richardson crater, Mars

François Andrieu, Frédéric Schmidt, Sylvain Douté, Eric Chassefière

# Ice state evolution during spring in Richardson crater, Mars

François Andrieu[1,2], Frédéric Schmidt[1], Sylvain Douté[3], Eric Chassefière[1]

[1] *GEOPS, Univ. Paris-Sud, CNRS, Université Paris-Saclay, Rue du Belvédère, Bât. 504-509, 91405 Orsay, France,* [2] *LESIA, Observatoire de Paris, PSL Research University, CNRS, Sorbonne Universités, UPMC Univ. Paris 6, Univ. Paris Diderot, Sorbonne Paris Cité, France,* [3] *IPAG, Univ. Grenoble Alpes, CNRS, F-38000 Grenoble, France*



**Abstract**

The Martian climate is governed by an annual cycle, that results in the condensation of $CO_2$ ice during winter, up to a meter thick at the pole and thousands of kilometers in extension. Water and dust may be trapped during the condensation and freed during the sublimation. In addition, ice may be translucent or granular depending on the deposition process (snow vs direct condensation), annealing efficiency, and dust sinking process. The determination of ice translucency is of particular interest to confirm or reject the cold jet model (also known as Kieffer model).

This work is focused on the dune field of Richardson Crater (72°S, 180°W)in which strong interactions between the water, dust and $CO_2$ cycles are observed. We analyzed CRISM hyperspectral images in the near IR using radiative transfer model inversion. We demonstrate that among the states of $CO_2$ ice, the translucent state is observed most frequently. The monitoring of surface characteristics shows a decrease in the thickness of the ice during the spring consistently with climate models simulations. We estimate a very low dust content of a few ppmv into the $CO_2$ ice, consistent with the formation scenario of cold jets. The water impurities is around 0.1%v, almost stable during the spring, suggesting a water escape from the surface of subliming $CO_2$ ice layer. The water ice grain size varies in a range 1 to 50 microns. From these results, we propose the following new mechanism of small water ice grain suspension: as a cold jet occurs, water ice grains of various sizes are lifted from the surface. These jets happen during daytime, when the general upward gas flux from the subliming $CO_2$ ice layer is strong enough to carry the smaller grains, while the bigger fall back on the $CO_2$ ice layer. The smaller water grains are carried away and integrated to the general atmospheric circulation.

*Keywords:* Mars, CO2 ice, radiative transfer, inversion, spectroscopy, seasonal south polar cap

## 1. Introduction

The Martian climate is mostly governed by a planetary scale $CO_2$ condensation-sublimation cycle. As the atmosphere is composed of 96% $CO_2$ (Mahaffy et al., 2013; Owen et al., 1977), the $CO_2$ cycle is the dominant climatic cycle (Leighton and Murray, 1966; Tillman, 1988; Mischna et al., 2003). The other two cycles that play important role in the martian climate are the dust cycle and the water cycle. General circulation models for Mars are now able to predict at a regional scale the amount of $CO_2$ ice present at the surface, but the water ice and dust cycles are still under-constrained. On Mars, climatic quantities such as $CO_2$ ice quantity at the surface are computed into boxes that are 3.75° in latitude and 5.25° in longitude (up to a few hundreds of kilometers). As approximately 30% of the atmosphere condenses at the surface during winter, the $CO_2$ cycle has a huge radiative impact on the planet and it is therefore of prime importance to be able to model it correctly.

One method to decipher the microphysics of the surface/atmosphere exchange involved in this cycle is to study the details of the reflectance response of the soil. Indeed, the full shape of the absorption bands contains informations about the surface and atmospheric properties. Not only the chemical composition (presence/absence of $CO_2$ or water ice) can be derived, but also the surface properties (grains size, abundances...). Various models have been proposed to simulate the reflectance of the Martian surface when covered with $CO_2$ ice (Douté and Schmitt, 1998; Appéré et al., 2011; Singh and Flanner, 2016), but a common point of those models is that they all considered that the ice deposits are granular, with a porosity close to 50%. Yet, defrosting spring activity (Piqueux et al., 2003; Kieffer et al., 2006; Hansen et al., 2013; Andrieu et al., 2014) strongly suggest that during most of the spring (defrosting season), the $CO_2$ ice layer is in fact in a translucent slab state. Then it is very important to be able to model the radiative response of such a surface, very different from a granular surface's response.

Recently, we have built a radiative transfer model able to simulate the near infrared reflectance of a surface constituted of a slab of $CO_2$ ice, clean or contaminated with water ice and mineral dust, and that lays on the Martian regolith (Andrieu et al., 2015). We also developed an inversion method, adapted to our study that we validated in a previous study: based on Bayesian formalism, the method uses a reference theoretical database to estimate a probability density function of the value of the parameters that are to be investigated(Andrieu et al., 2016). The combination of the inversion method with the radiative transfer model allows to retrieve ice covered surface properties from their near infrared spectrum. The properties retrieved are the thickness of the ice layer, and the proportions and grain sizes of impurities. These tools allow us to follow the volatiles

exchanges between the Martian surface and atmosphere during spring, to bring better constraint to the seasonal Martian climatic cycles.

This study focuses on the dune field inside Richardson Crater (180°W, 72°S). This dune field was widely studied (Mohlmann and Kereszturi, 2010; Kereszturi et al., 2011; Supulver et al., 2001; Edgett et al., 2000; Martinez et al., 2012) because it showed intense spring activity and interactions between water and $CO_2$ cycle.

In this work we:

- argue about the presence/absence of translucent $CO_2$ ice.
- determine the surface properties of the seasonal frost (thickness, grain-size, dust impurities, water impurities)
- propose a microphysical model to describe the exchanges of volatiles in Richardson crater

## 2. Method

In this work we compare real data with synthetic data to perform an "inversion". To produce realistic synthetic data, we first need a realistic direct model described in subsection 2.1. Among the initial inputs of this model are the optical indexes of the species constitution the surface. Optical indexes for ices are documented in the literature (Schmitt et al., 1998), but are unknown for Martian dust. Therefore, we estimated them from spectral measurement, as described in subsection 2.2. Then the direct model and its inversion will be described. The final step is the inversion method used to get information from the comparison of our synthetic spectra with real data, detailed in the last section 2.3.

### *2.1. Direct model*

*Granular ice.* The radiative transfer model used to simulate the spectra in the case of a translucent ice is semi analytic (Douté and Schmitt, 1998), as used to determine seasonal cap properties (Appéré et al., 2011). The surface is supposed to be constituted of a semi infinite layer (i.e. optically thick) that represents the $CO_2$ deposit, contaminated with water ice and dust. The model uses as initial input: (i) the optical constants used for the $CO_2$ and water ice are from (Schmitt et al., 1998), and the optical constants of the regolith were estimated from summer measurements (see previous section) (ii) the grain-sizes (iii) the proportions of each type of impurity present in the ice layer.

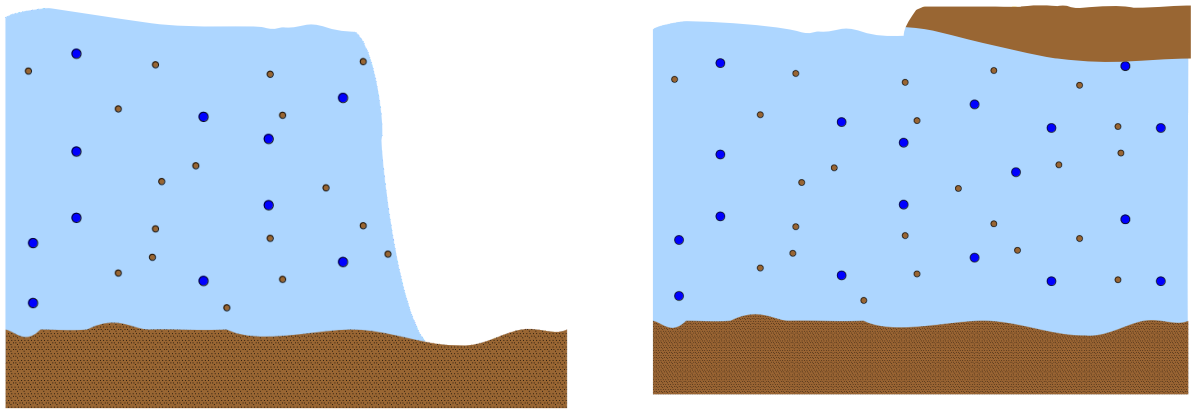

(a) (b)

Figure 1: Model of the surface: a slab of $CO_2$ ice, possibly contaminated with water ice and regolith dust lays on the top of the lambertian regolith. A sub-pixel linear mixing of two different surface is possible to model (a) the possibility of completely defrosted patches within a pixel or (b) an optically thick layer of dust covering the ice. Both situations result in the same modeled spectrum.

*Translucent ice.* The radiative transfer model used to simulate the spectra in the case of a translucent ice is semi analytic (Andrieu et al., 2015). The model uses as initial input: (i) the optical constants of the materials constituting the surface: $CO_2$ and water ice from laboratory measurements (Schmitt et al., 1998), and dust from previous consideration, (ii) the thickness of the upper ice layer, (iii) the roughness of the upper surface, (iv) the grain-sizes and (v) the proportions of each type of impurity present in the ice layer and (vi) the single scattering albedo of the underlying regolith, that is supposed to be a semi-infinite and lambertian. The number of impurity types that can be introduce in the model is not limited in theory, but practically, it is not possible to introduce more than two different types due to computation limitations.

*Linear mixture of defrosted terrain.* In order to take into account the presence of defrosted area within one CRISM pixel, we allow a linear mixture of regolith with the previous ice model (see fig. 1). Thus, one extra parameter will be estimated: the surface proportion of naked terrain. This possibility of sub-pixel geographical mixing appears even at the spatial resolution of the CRISM instrument, of about 20 m per pixel, if a mixture occurs within the same pixel. It is also possible that, following ejections, an optically thick layer of dust covers the layer of ice locally (see Figure 1). These two possibilities are described in exactly the same way, considering a linear mixture between a surface described by the radiative transfer model (Andrieu et al., 2015), and a surface consisting only of regolith.

### *2.2. Optical indexes of the Martian dust*

The martian southern dust differ from the northern one and from regular palagonite (Douté et al., 2007). We may estimate the optical indexes analyzing a defrosted area, with some assumptions. Contrary to this previous work, we did not assume a lambertian surface for the dust and correct for the photometric effect in order to estimate the reflectance in a normal geometry.

#### *2.2.1. Single scattering albedo of the regolith*

Using the Hapke reflectance model (Hapke, 1984), we inverted reflectance spectra of the ice free surface measured by the CRISM instrument to estimate the single scattering albedo $\omega(\lambda)$, that can be easily converted into normal reflectance. The goal is to find the parameter $\omega(\lambda)$, assuming the other fixed parameters, taking the average martian photometric parameters given by Vincendon, 2013, *i.e.* $\theta = 17$, c = 0.6, b = 0.12, $B_0 = 1$ and h = 0.05. The estimation is performed by a bayesian inversion, for which we consider each wavelength independently (Fernando et al., 2013, 2015; Schmidt and Fernando, 2015). The solution is a probability density function (PDF) of $\omega$ that can be reduced by its mean $\langle\omega\rangle$, dependent on the wavelength.

The measured spectra data can be modeled with these photometric parameters and with a relatively small uncertainties on $\omega$ (less than 0.05). Moreover, it can be noted in the figure 2 that the result is very stable as a function of the wavelength, which is a guarantee of the quality of the inversion, because each wavelength has been inverted independently.

#### *2.2.2. Optical indexes of the Martian dust*

The Shkuratov et al., 1999 model is an inverse analytical model (with an inverse analytical form) of one-dimensional geometric optics, under normal conditions of incidence and emergence. Assuming the real part of indexes, the size of the grains, the porosity of the surface and knowing the value of the reflectance from the previous step, we estimate the imaginary part $k_n$ of the optical index. We fix the value for porosity of the surface at 0.5, which is the classical value for this type of surface (Hapke, 2012). For the real part of its optical index and the size of its grains, we know the order of magnitude, but not the precise values. We have generated optical indexes by assuming grain sizes varying from $10\,\mu$m to $30\mu$m and real parts of the optical indexes ranging from 1.3 to 1.9. Using Shkuratov's inverse analytic model, we can generate the PDF of $k_n$ from the PDF of reflectance (see figure 2). There is an increase of $k_n$ with the wavelength and the uncertainties are increasing, but remain relatively low, around 0.001. The grain-size has a much bigger

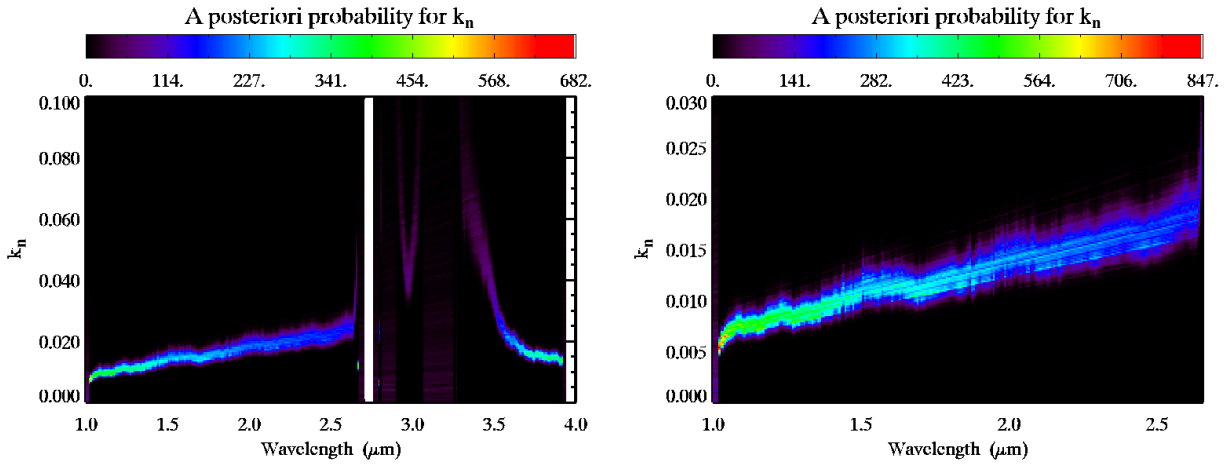


(a) (b)

Figure 2: (a) Distribution of the values (PDF) of the imaginary part of the optical index $k_n$, calculated from the values of $\omega$ of the Markov chains obtained after the Bayesian inversion, considering a grain size of 30 $\mu$m in the Shkuratov model. We thus propagate the distribution of the values of $\omega$ on the values of $k_n$. These values being determined from the calculation of the single diffusion albedo $\omega$, the same discontinuities are observed, and it is not possible to calculate a value for a wavelength situated in an absorption band of the $CO_2$. (b) Zoom on the part of interest located between $1\mu m$ and $2.6\mu m$ of the distribution of the values of the imaginary part of the optical indices $k_n$, obtained from the values of $\omega$ of the Markov chains. We see that just like the distribution of $\omega$, the distribution of the values of $k_n$ also often admits two maxima. The value that has been retained is the average value of this distribution.

impact on the form of the spectrum of $k_n$ than the real part of the optical index. If we compare the values of the $k_n$ calculated from the OMEGA (Douté et al., 2007) or CRISM data, using the same values for the other parameters (real part of the optical index, grain size, compactness), very close results are obtained, demonstrating the robustness of the method regarding the input data. The grain size is not constrained. Since each grain size has coherent optical index, it is impossible to distinguish those two parameters. We choose a grain size of 30 $\mu$m arbitrarily. It is close to the typical martian dust (Kieffer, 2007; Vincendon et al., 2009; Forward et al., 2009). In the following the retrieved dust content will be subject to this indetermination.

### *2.3. Inversion*

The inversion methods has been validated in a previous study (Andrieu et al., 2016). The principle is to build a spectral lookup table using the radiative transfer model, and to find a solution to the inverse problem using bayesian statistics. The solution is a probability density function (PDF) that is defined in the parameters space. The likelihood $L$ is estimated for each spectrum in the look up table (LUT), with:

$$L = \exp\left(-\frac{1}{2} \times {}^{t}\left(d_{sim} - d_{mes}\right) \overline{\overline{C}}^{-1} \left(d_{sim} - d_{mes}\right)\right) \tag{1}$$

where $d_{sim}$ is a simulated spectrum from the LUT, $d_{mes}$ is the data, $^t$ is the transpose operator that applies to $(d_{sim} - d_{mes})$, and $\overline{\overline{C}}$ is the covariance matrix that represent the uncertainties on $d_{mes}$. $d_{sim}$ and $d_{mes}$ are $n_b$ elements vectors corresponding to respectively simulation data and measurements data, with $n_b$ the number of spectral bands used ($n_b = 247$).

Therefore, $\overline{\overline{C}}$ is a $n_b \times n_b$ matrix, where each eigenvector represents a source of uncertainty, and the associated eigenvalue represents the level of uncertainty. Usually this matrix is assumed to be diagonal with the noise level variance on the diagonal element. In our case, we introduced the uncertainties due to the atmospheric correction: the shift and general slope that may be introduced by variations of geometry at the surface, accentuated by the atmospherical corrections (see Fig. 5). We represent it by two eigenvectors $\vec{t} = \frac{1}{n_b}(1, ..., 1)$ and $\vec{s} = \frac{\vec{S}}{\|\vec{S}\|}$, with $\vec{S} = \left(-\frac{n_b-1}{2}, \ldots, -2, -1, 0, 1, 2, \ldots, \frac{n_b-1}{2}\right)$. $\vec{s}$ characterizes the spectral slope value, and $\vec{t}$ characterizes the ordinate at the spectral shift. As $\overline{\overline{C}}$ must be a positive definite matrix, $\vec{s}$ and $\vec{t}$ must be orthogonal, so the formulation of $\vec{s}$ is imposed by $\vec{t}$. The 245 other eigenvectors represent the noise, and are build using the Gram-Schmidt process. In the basis constituted of the eigenvectors, $\overline{\overline{C}}$ is diagonal and its diagonal elements are the eigenvalues $\sigma_1^2$, $\sigma_2^2$ and 245 times $\sigma_3^2$ , where $\sigma_1$ and $\sigma_2$ respectively represent a standard deviation associated to $\vec{t}$, $\vec{s}$, and $\sigma_3$ represent the standard deviation associated to the noise. We chose $\sigma_1 = \sigma_2 = 0.02$ and $\sigma_3 = 0.03$, in agreement with our analysis.

The likelihood computed are then converted to *a posteriori* probability density functions (PDF). For the parameter $m_i$ of the radiative transfer model, the a posteriori PDF is:

$$\mathcal{P}\{m_i\} = \frac{\mathrm{L}(m_i)\,\mathrm{d}p(m_i)}{\sum_i \mathrm{L}(m_i)\,\mathrm{d}p(m_i)} \tag{2}$$

where $\mathrm{d}p(m_i)$ is the differential element at the sampling point $m_i$ of the parameters space $M$: $\mathrm{d}p(m_i) = \prod_j \partial p_j(m_i)$. To make the solution easier to read, marginal a posteriori PDF are built: the PDF is projected on one parameter's axis. This allow the visualization of the solution for a given parameter $p_j$ in a graph. For the parameter $p_j$, there are $n_j$ sampling steps that are represented by the letter $k$ ($k$ in Eq. 3 ranges from 0 to $n_j$). The marginal a posteriori PDF for $p_j$ at the sampling step $k$ is:

$$\mathcal{P}\{p_j(k)\} = \frac{\mathrm{L}'(k)}{\sum_i \mathrm{L}'(k)\,\partial p_j(k)} \tag{3}$$

with $\partial p_j(k)$ the differential element for $p_j$ at $k$, and:

$$\mathrm{L}'(k) = \sum_i \mathrm{L}(m_i \mid p_j(k)) \prod_{l \neq j} \partial p_l(m_i \mid p_j(k)) \tag{4}$$

| Parameter | Values sampled | Number of sampled values |
|---|---|---|
| Thickness of the $CO_2$ slab(mm) | $0$ ; $0.01$ ; $0.05 - 1$ in steps of $0.05$ ; $1 - 200$ in steps of $1$ ; $200 - 300$ in steps of $5$ ; $300 - 1000$ in steps of $50$ | 250 |
| Total amount of impurities (%) | $0$ ; $0.005$ ; $0.01$ ; $0.05 - 1$ in steps of $0.05$ ; $10 - 100$ in steps of $10$ ; $10 - 100$ in steps of $10$ | 32 |
| Dust proportions among impurities (%) | $0$ ; $1$ ; $10$ ; $50$ ; $90$ ; $99$ ; $100$ | 7 |
| Water ice proportions among impurities (%) | $0$ ; $1$ ; $10$ ; $50$ ; $90$ ; $99$ ; $100$ | 7 |
| Water ice grain diameter ($\mu$m) | $1$ ; $3$ ; $10$ ; $30$ ; $100$; $300$ ; $1000$; $3000$ ; $10000$ ; $30000$ | 10 |
| Surface proportion of dust in linear mixing (%) | $0 - 100$ in steps of $10$ | 11 |
| Incidence | $55° - 80°$ in steps of $5°$ | 6 |
| Emergence | $0° - 30°$ in steps of $10°$ | 4 |
| Azimuth | $60°, 150°$ | 2 |

Table 1: Values sampled in the LUT for the translucent slab model.

### *2.4. Look Up Tables (LUT)*

The LUT must make it possible to sample the space of the parameters in an optimal way: representative way not to miss any information, but not too voluminous to avoid making the calculations more complicated. A series of tests was therefore carried out, traversing the space coarsely following a logarithmic sampling to locate where in the parameters space there is most variability. As we do not know precisely the optical constants of the Martian regolith, it is useless to try to find the size of the grains. To maintain maximum consistency, this parameter was not sampled. The set of values sampled in the synthetic LUT is summarized in the table 1 for the slab ice model, and in the table 2 for the granular ice model.

This synthetic LUT for the slab model contains 9939264 spectra, corresponding to 207068 configurations of different surfaces for 48 geometries of measurements, representing the variability of the direct model. Each spectrum was calculated at high spectral resolution (29037 wavelengths at a spectral resolution of about $0.5\,\mathrm{cm}^{-1}$), and then resampled at the resolution of the CRISM instrument (247 wavelengths used here, at a resolution of 6.5 nm), using the transfer function of the sensor. It was computed in 60 h, in parallel on four Intel Xeon CPU cores Xeon E5640, 2.66 GHz.

To take the sub-pixel mixture into account during the inversion, the LUT is extended by calculating the mixture with a martian dust spectrum at the corresponding geometry and for the different desired surface ratios. In this study, we sampled 11 values of surface proportions of linear mixing with dust, ranging from 0

| Parameter | Values sampled | Number of sampled values |
|---|---|---|
| Grain diameter of $CO_2$ ice ($\mu$m) | 1 ; 3 ; 10 ; 30 ; 100 ; 300 ; 1000 ; 3000 ; 10000 ; 30000 ; 100000 ; 300000 | 12 |
| Total amount of impurities (%) | 0 ; 0.005 ; 0.01 ; $0.05-1$ par pas de 0.05 ; $10-100$ in steps of 10 ; $10-100$ in steps of 10 | 32 |
| Dust proportions among impurities (%) | 0 ; 1 ; 10 ; 50 ; 90 ; 99 ; 100 | 7 |
| Water ice proportions among impurities (%) | 0 ; 1 ; 10 ; 50 ; 90 ; 99 ; 100 | 7 |
| Water ice grain diameter ($\mu$m) | 1 ; 3 ; 10 ; 30 ; 100; 300 ; 1000; 3000 ; 10000 ; 30000 | 10 |
| Surface proportion of dust in linear mixing (%) | $0-100$ in steps of 10 | 11 |
| Incidence | $55^\circ-80^\circ$ in steps of $5^\circ$ | 6 |
| Emergence | $0^\circ-30^\circ$ in steps of $10^\circ$ | 4 |
| Azimuth | $60^\circ, 150^\circ$ | 2 |

Table 2: Values sampled in the LUT for the compact granular layer model Douté and Schmitt.

to 100 in steps of 10. The LUT compared to the data during the inversion is thus 11 times more voluminous than that described previously, and therefore contains a total of 109331904 spectra, corresponding to 2277748 different surface configurations.

## 3. Data

### *3.1. CRISM data*

The CRISM instrument (Murchie et al., 2007) has well covered the Richardson Crater area, and provide 12 cubes of the same area for the spring martian year 28. This time coverage is enough to follow the general time evolution of seasonal deposits through spring: the mean time span between two acquisitions is 9° of solar longitude, or 16.7 *sols*. Another advantage of the CRISM data is that most of the observations are coupled with HiRISE images (McEwen et al., 2007) of the same area, taken at the same moment, at a resolution of 25cm/px. This allows to investigate closely the relations between spectroscopic and spatial informations. In particular, the dark dune spots, widely active in the area (Kereszturi et al., 2011) have a spatial extension of a few CRISM pixels, and thus their evolution can be monitored both spectroscopically using CRISM and geomorphologically using HiRISE data.

The purpose of this work was to investigate precisely the interactions between surface and atmosphere during the spring defrosting in areas that show defrosting spring activity. These spring defrosting manifestations

have a typical scale of a few hundreds meters to a few kilometers. The resolution of the instrument used to study them shall then be lower than a hundred meters. We thus chose the instrument CRISM that provide the best possible spatial resolution (approx. 20m per pixel) compared to others imaging spectrometers. Moreover, CRISM acquires data always at the same local solar time, so diurnal variations are not to be taken into account.

We searched for areas of particular interest, that presented a time coverage by CRISM that was sufficient to follow the evolution of the seasonal deposits. We chose the Richardson crater dune field (See Figure 3) for the following reasons:

1. The time sampling by CRISM was sufficient for the spring of martian year 28 (12 data cubes available).
2. The area is fully covered by $CO_2$ ice at the beginning of the time series and fully defrosted at the end.
3. This area showed an intense surface process activity.
4. Several previous studies demonstrated the abundant presence of water ice in this area, suggesting possible interactions between water and $CO_2$ cycles, and justifying the use of complex radiative transfer simulations to model the radiation in the surface.

The 12 available CRISM cubes for this area are summarized in table 3. The first cube of the spring (HRS0000411F) turned out to be ineffective, because a large number of bands were saturated in atmosphere due to the high incidence angle and because of the generally low albedo of the surface. From Ls=251° and after, no $CO_2$ ice can be detected at the surface using band criterion methods (Langevin et al., 2007), meaning the the seasonal ice deposits have completely sublimed.

In the area, we chose to focus on a few different spots, and to investigate deeply their evolutions. We used the combined HiRISE and CRISM data to select a few "control points", where no dark spot of flow activity is recorded during the spring, and some point precisely where a dark spot appears (See Figure 3 and 4 for details). The temporal series of spectra corresponding to each study area were then extracted from the CRISM cubes.

### *3.2. Noise level*

The nominal CRISM instrumental noise is very low, and still was at the time when the data were acquired (2007), with a signal to noise ratio between 400 and 500 depending on the wavelength. Nevertheless, the real data show a level far higher, most probably due to detector electronics, atmospheric perturbations, or geometric variations within a pixel. Computing the covariance matrix of a set of spectra that are supposed to

| Cube ID | Acquisition date | $L_S$ (°) | AOT | Mean solar incidence (°) | Comments |
|---|---|---|---|---|---|
| HRS0000411F | 30/01/2007 | 175.213 | n. c. | 83.9 | Atmosphere saturated |
| HRL000043A2 | 10/02/2007 | 181.550 | 0.59 | 80.9 | $CO_2$ and water ice at the surface |
| HRS000049E5 | 09/03/2007 | 197.016 | 1.11 | 75.9 | $CO_2$ and water ice at the surface |
| FRT000052BC | 05/04/2007 | 213.719 | 0.92 | 69.1 | $CO_2$ and water ice at the surface |
| FRT000054E5 | 12/04/2007 | 217.503 | 0.72 | 66.7 | $CO_2$ and water ice at the surface |
| HRS000056C0 | 17/04/2007 | 220.683 | 0.43 | 66.1 | $CO_2$ and water ice at the surface |
| FRT00005AF7 | 15/05/2007 | 238.066 | 1.32 | 60.2 | $CO_2$ and water ice at the surface |
| FRT00005C94 | 20/05/2007 | 241.319 | n. c. | 59.8 | $CO_2$ and water ice at the surface |
| FRT00005E38 | 26/05/2007 | 245.220 | 1.17 | 57.9 | $CO_2$ and water ice at the surface |
| FRT00005FF6 | 31/05/2007 | 248.483 | 1.32 | 57.6 | $CO_2$ and water ice at the surface |
| FRT00006102 | 04/06/2007 | 251.104 | 1.51 | 59.0 | No $CO_2$ ice at the surface |
| FRT00006C56 | 25/07/2007 | 283.403 | 2.1 | 53.7 | No $CO_2$ ice at the surface |

Table 3: Summary of available CRISM data for Richardson crater dune field, and for martian year 28. Dust aerosol optical thicknesses (AOT) are given by M. J. Wolff (Wolff et al., 2009). «n. c.» (not calculated) means M.J. Wolff's algorithm could not retrieve the dust AOT. Aerosols effect were not corrected in this case. Incidences are defined with respect to the Areoide.

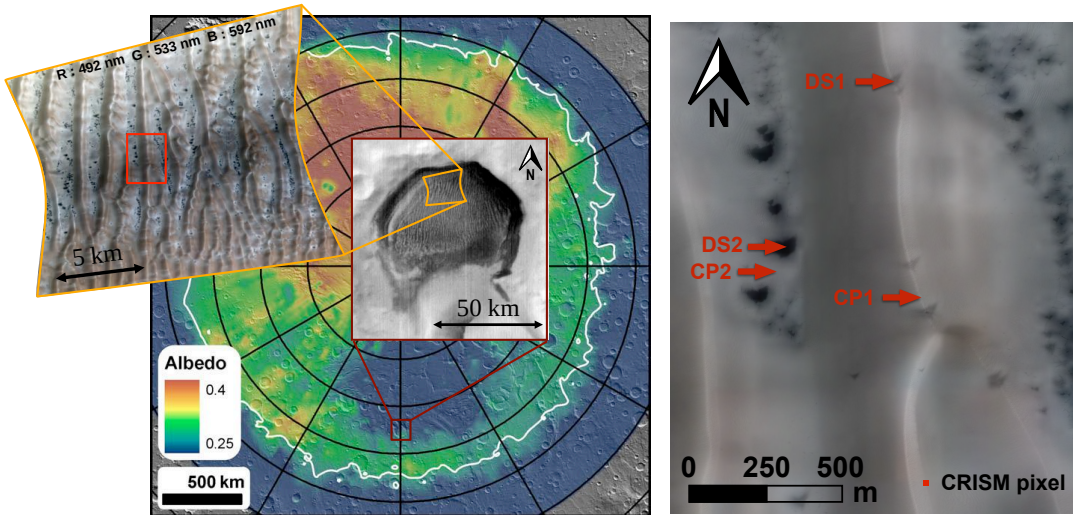


(a) (b)

Figure 3: (a) localization of Richardson crater, Mars. The back is a polar projection map centered on the south pole of Mars, from (Hansen et al., 2010), where the limit of the seasonal $CO_2$ ice deposits in the middle of the spring ($220° < Ls < 225°$) is represented in white. A MOC image of Richardson crater, located at 72.6°S, 180.4°W, is superimposed, and then a map projected color composition of a CRISM cube FRT000052BC (LS=213°). (b) Detail of areas of particular interest: extract from the CRISM color composition in (a) superimposed on an extract from HiRISE image PSP_002542_1080. Two control points (CP1 and CP2) and two points of particular interest that show defrosting activity (DS1 and DS2) were defined.

be close to identical allowed us to estimate that level of noise at approximately 3% of the signal, consistently with previous studies (Ceamanos et al., 2013; Fernando et al., 2013).

### *3.3. Atmospheric correction*

The atmospheric gas contribution was corrected using *ab initio* line by line radiative transfer calculations(Douté, 2014), based on general circulation models (GCM) predictions (Forget et al., 1999; Forget et al., 2006). The mineral aerosols atmospheric contribution was corrected using aerosols optical thickness (AOT) estimations by Wolff et al., 2009 and the method developed by Douté et al., 2013, that take into account the radiative coupling between gas and aerosols. No correction method has proven 100% efficient to remove the aerosols contribution for $CO_2$ ice covered areas (Vincendon et al., 2007, 2008; Smith, 2009; Wolff et al., 2009; Ceamanos et al., 2013; Douté et al., 2013; Douté, 2014). Therefore, we expect correction errors, that have to be taken into account in the inversions. We chose to estimate that level of error, and to introduce it in the inversion framework as a source of uncertainty.

As shown on figure 5, the atmospheric corrections may introduce a bias in the data in case of a sloped facet: in this graph are represented two spectra from the same region during summer. The whole area is homogeneously covered in dust and thus is not expected to show any spectral variability. The variability here is correlated with photometry, and thus attributed to a bias in atmospherical corrections. The bias as been

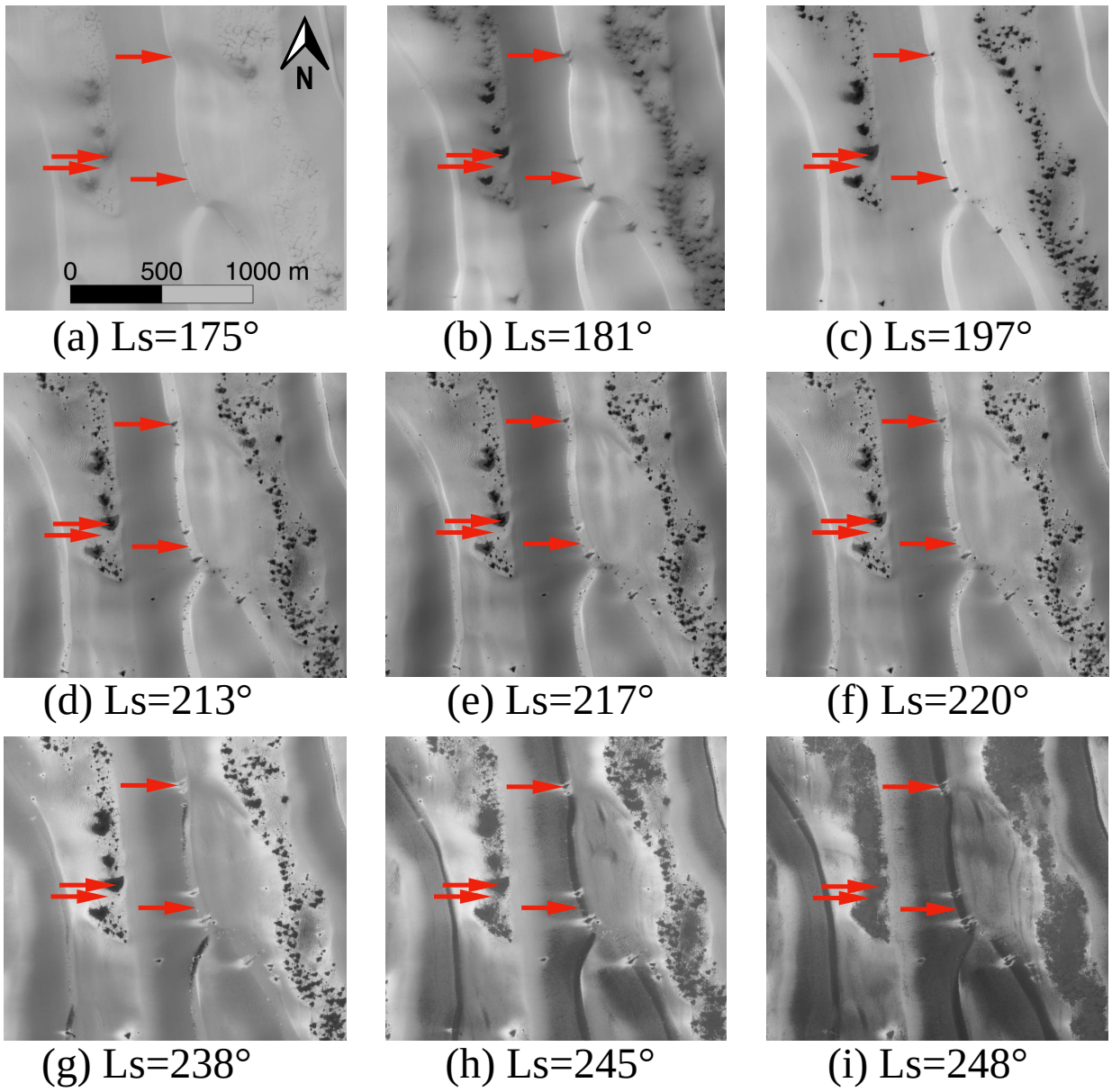


Figure 4: HiRISE series of the area of particular interest defined in Figure 3b, during the spring of MY28. Red arrows indicate the positions of the points CP1, CP2, DS1 and DS2 defined in figure 3b.

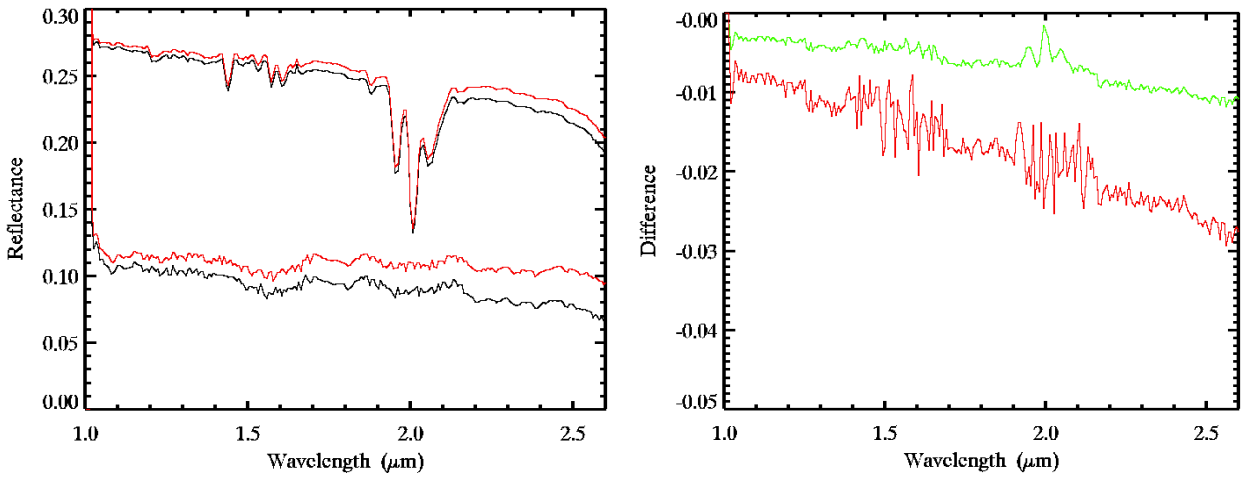


(a) (b)

Figure 5: Effect of local slopes at the surface, not taken into account in the atmospheric corrections (Douté et al., 2013). (a) Two spectra that are supposed to be identical before (up) and after (down) atmospheric corrections. The black lines represent the spectra before and after correction in a flat area, and the red ones in a slope. (b) Difference between the two supposed identical spectra (red spectra minus black spectra from fig. a), before (green) and after (red) atmospherical correction. There is a difference between the two supposed identical spectra, and the atmospherical corrections seem to enhance it, by adding a general spectral slope to the data.

estimated to be a general negative spectral slope of maximal magnitude of 0.01UR/µm (UR mean units of reflectance factor, that is dimensionless) but also a shift in the absolute level in the order of 0.02 UR. The covariance matrix of the uncertainties $\overline{\overline{C}}$ has to take these effects into account.

## 4. Results

### *4.1. Best fit*

The inversion method described above takes into account the fact that the reflectance spectrum of the surface may be slightly deformed by a spectral slope and level due to imperfect atmospheric correction. It is crucial to avoid interpreting these deformations in terms of composition and surface condition erroneously. Not only this potential bias is ignored by the inversion algorithm thanks to the first two eigenvectors of $\overline{\overline{C}}$ (see section 2.3), but it is estimated and can therefore be corrected from the data. The adjustments shown in the figures 6 and 7 were done by correcting this bias according to the level estimated by the inversion algorithm. As demonstrated by these figures, the best fits are usually in very good agreement with the data. The worst is the first, due to spikes at wavelengths around 1.7 $\mu$m and 2.2 $\mu$m in the observations that are most probably artifacts.

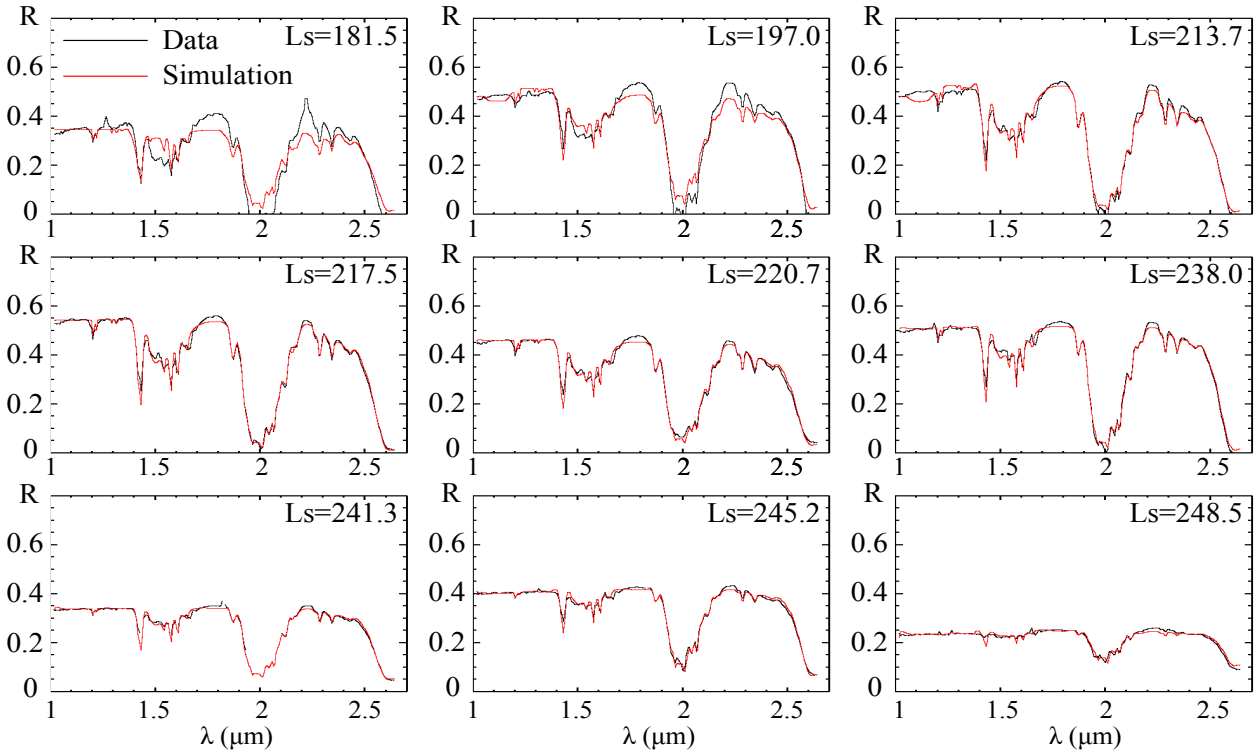


Figure 6: Best fit of translucent ice model as a comparison with the data for temporal series of point CP1 from $L_S = 181.5°$ to $L_S = 248.5°$. The best fit spectra are re-adjusted at the level of deformation estimated by the inversion.

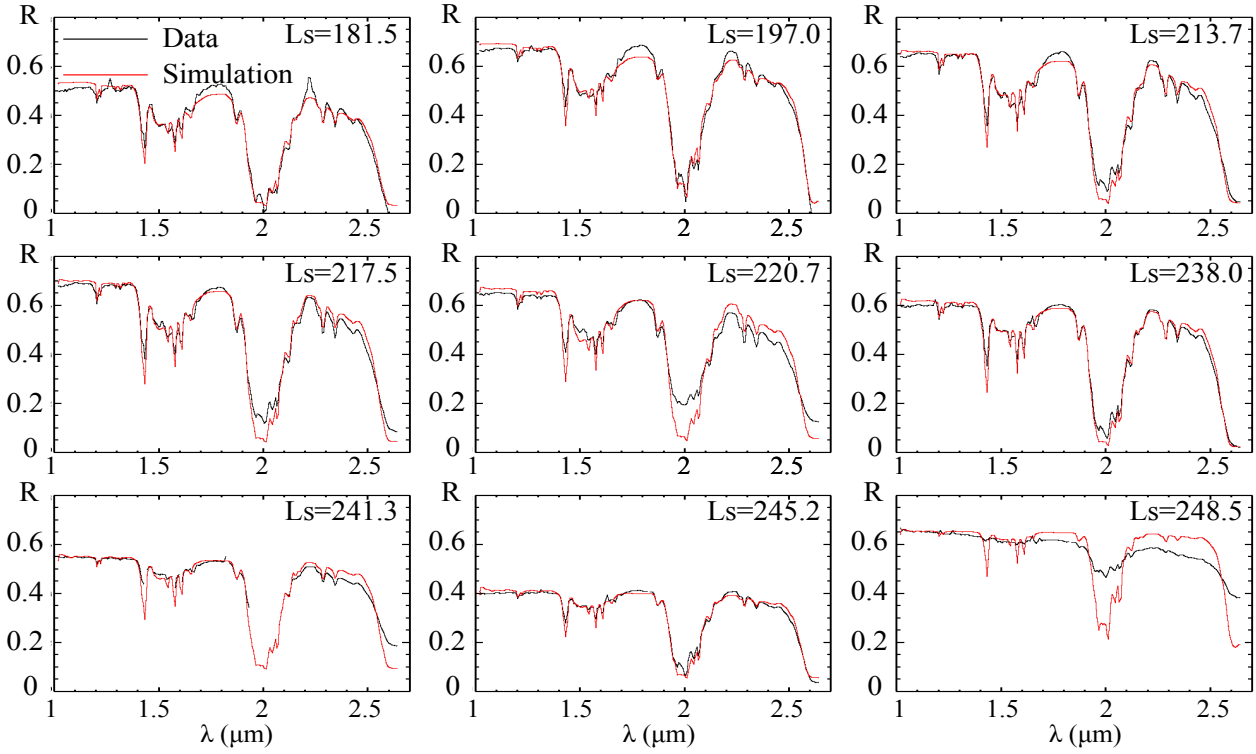


Figure 7: Best fit of granular ice model as a comparison with the data for temporal series for CP1 from $L_S = 181.5°$ to $L_S = 248.5°$. The best fit spectra are re-adjusted at the level of deformation estimated by the inversion.

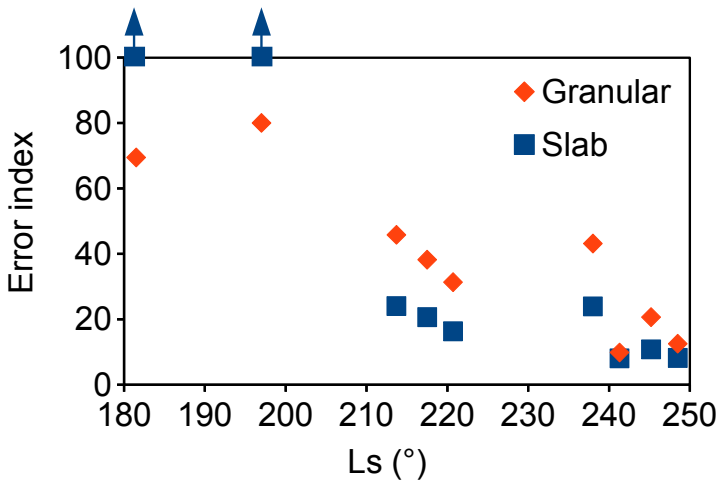


Figure 8: Error indexes ($EI$) of the fits for point CP1 for the slab and granular models

*4.2. Slab vs granular ice*

Both slab ice or granular ice models fit reasonably well the data. Therefore, the quality of the fit will not be determinant to decide which model is closer to reality. Figure 8 shows an error index $EI = |\ln L|$, where L is the likelihood. Thus high value of $EI$ means bad fit, and $EI = 0$ means a perfect fit. In terms of error index, the granular model fits better (even if badly ) for the first two measures of the season, and then the slab model have a lower error index. Nevertheless both models show an error index of similar magnitude. The quality of the fit then is inappropriate to discriminate the models. To test the coherence of these model, we compare them with other independent estimates. Predictions of $CO_2$ ice quantity (in kg.m$^{-2}$) at the surface by climate models are readily available via the Mars Climate Database [1] (Lewis et al., 1999; Forget et al., 1999; Forget et al., 2006; Millour et al., 2012; Millour et al., 2014). The thicknesses are then deduced from the GCM prediction by considering an homogeneous layer, and mass density of 1606 kg.m$^{-3}$ (Kieffer, 2007; Thomas et al., 2011). The thickness data derived from the climate models are then plotted in the graphs with ice thickness estimates in Fig. 9. We can see in the figure 9 that the direct estimates realized with our algorithm and the predictions from the climate models are consistent. Similar orders of magnitude, and often very close estimates are observed, except for Ls = 181.5°, where we observe thicknesses clearly greater than those predicted.

For the granular ice model, we can estimate the minimum thickness of granular ice required for a optically thick layer. Since the ice is poorly absorbent, a layer of 10 grains is required to fulfill this property (see fig. 9).

[1] http://www-mars.lmd.jussieu.fr/mcd_python/

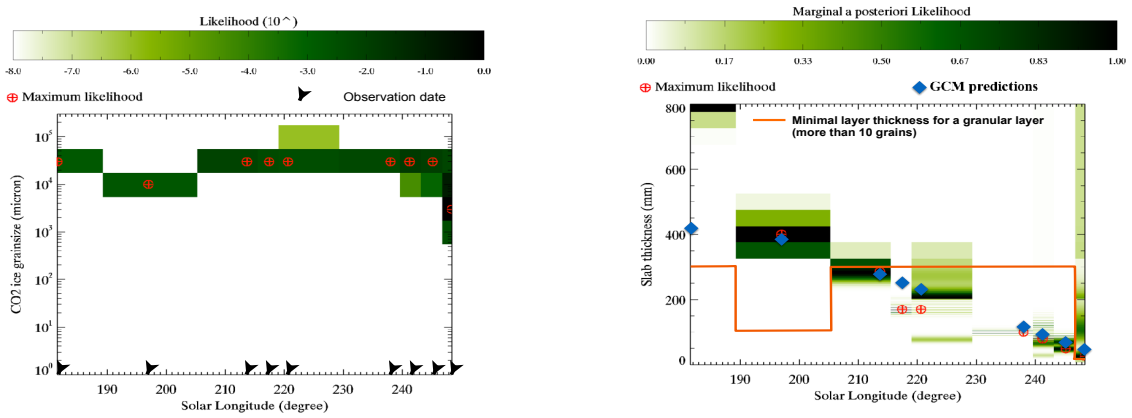


(a) Granular

(b) Slab

Figure 9: (a) Evolution of the grain size in a granular ice layer case for CP1. The shades of green represent the values of the marginal a posteriori of the likelihood PDF, and the red crosses point out the maximum value of the likelihood PDF (best fit), at each observation date. (b) Evolution of the thickness of the ice layer as a function of Ls for CP1, in the case of a slab layer. The GCM predicted evolution (Millour et al., 2014 ©LMD/OU/IAA/ESA/CNES) has been added in blue diamonds, considering a density for $CO_2$ ice of $\rho = 1606\,\mathrm{kgm}^{-3}$ (Kieffer, 2007), and the minimal thickness possible for a granular layer, derived from the grain-diameters given by figure a have been added in red.

We can thus compute the minimum thickness in the case of a granular ice that is inconsistent with the MCD, even with the expected behavior of sublimating. The grain diameter in the case of a granular model shows no clear evolution during spring (see figure 9a), and figure 9b shows that the minimum thickness required to fulfill the granular model assumptions is highly inconsistent with the climate models predictions. On the contrary, the thickness estimates from the slab ice models show a decrease during spring in agreement with the values predicted by the Mars Climate Database. From this result, the granular ice can be ruled out and be ignored for the rest of this article.

### *4.3. Thickness*

As a general rule, the thickness estimated by the inversion algorithm for the ice layer decreases during spring, as is naturally expected. Figure 10 presents the temporal ice thickness for the four points of our study from early to late spring. They represent on the same graph the posterior marginal probability density values (eq. 3) for each inversion.

All points are following the expected sublimation process. One can note a local variability of the thickness, on a scale that is not taken into account by the GCM: the ice layer is thicker on the crests of dunes (CP1) and thinner in the inter-dunes (CP2), which is expected. Indeed, the inter-dunes show polygonal cracks (see Fig. 3b), indicating possibly the presence of permafrost, and most probably a water ice rich subsurface with a high thermal inertia. Conversely, the dune is constituted of sand, with small grains with low thermal inertia.

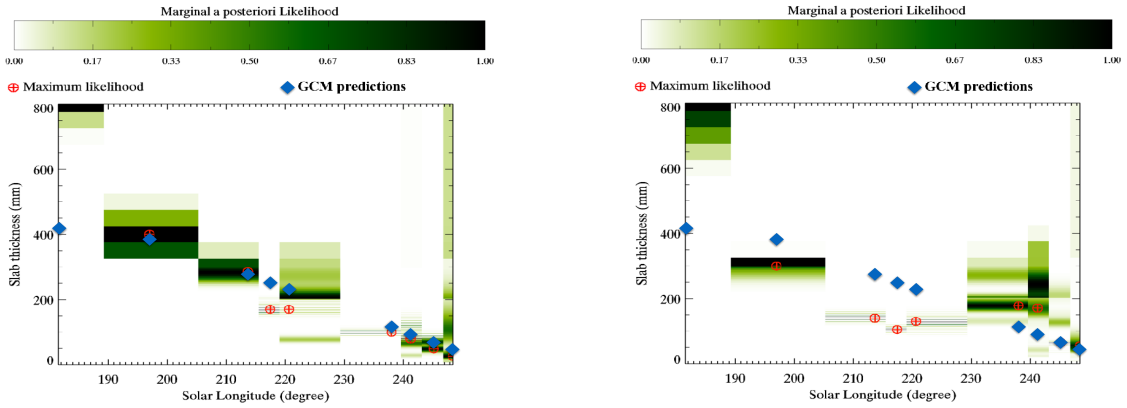


(a) Point CP1




(b) Point CP2

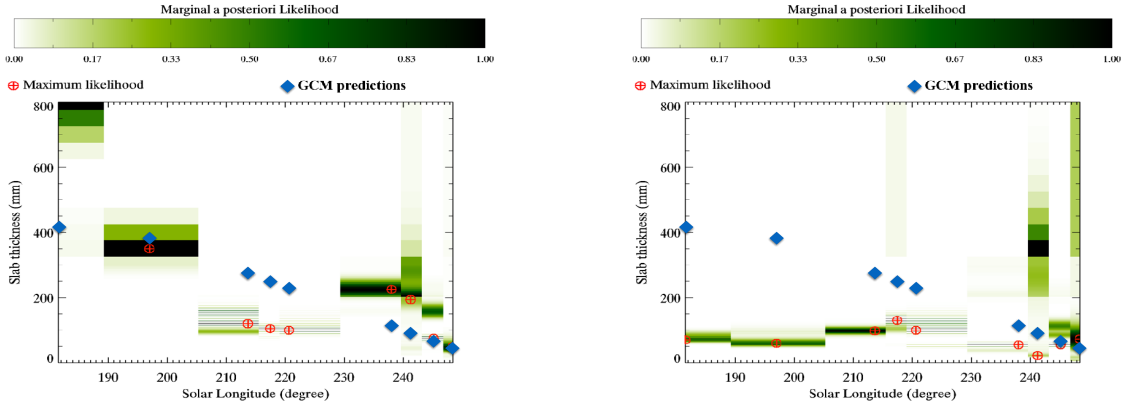


(c) Point DS1




(d) Point DS2

Figure 10: Evolution of the thickness of the top slab ice layer as a function of Ls for (a) CP1 (b) CP2, (c) DS1 and (d) DS2. The shades of green represent the values of the marginal a posteriori of the likelihood PDF, and the red crosses point out the maximum value of the likelihood PDF (best fit).

A terrain with high thermal inertia will start to condense $CO_2$ much later, and the dune will therefore start the spring with a much thicker $CO_2$ ice layer than the inter-dunes.

At the center of the dark spots, the thickness of the layer is lower than that of the surrounding areas (the thicknesses at CP1 are compared with those of DS1 and the thicknesses of CP2 with those of DS2), which is consistent with the mechanism of cold jets proposed by Piqueux et al., 2003 and Kieffer et al., 2006: it is expected that the ice breaks where it is most fragile, where the thickness of the layer is the lowest. Alternatively, the points in the dark fans DS1 and DS2 could have a lower slab thickness due to the enhanced sublimation due to darker albedo because of the covering dust. In the dark spots of the inter-dune, the thickness of the layer is low from the beginning of spring, which is consistent with the activity of jets much earlier in these zones (see fig. 3b), as seen by Pommerol et al., 2013 in the north. These are illuminated longer during the day than the slope zones (the slopes are oriented towards the east or the west) from the end

of the polar night, and the greater roughness of the inter-dune zones compared to the smooth zones of the slopes favor a more important basal sublimation, and thus the activity is early (Pommerol et al., 2013). It should be noted that the thickness remains almost constant throughout the season, which is consistent with an effect due to contamination by water ice proposed by (Pommerol et al., 2013), and that will be discussed in section 4.4. In detail, DS1 and DS2 have a peculiar behavior that thickness is decreasing from Ls=181.5 to Ls=210-220 and then increase to finally decrease. We attribute this apparent thickening of the ice to the dust migration within the ice, producing a optically thick layer of dust migrating downwards.

### *4.4. Contamination*

#### *4.4.1. Impurities proportions*

The total impurity content of the ice layer corresponds to the sum of the volume proportions of water ice and dust in the matrix. As can be seen in figure 11, this content seems to remain relatively stable between 0.01 % and 0.1% for the all points. The total budget of impurities has to be investigated conjointly with the respective proportions of dust and water ice among them, represented on figure 12. For all the points studied, dust contamination seems very low. Indeed, the relative proportions between water ice and dust estimated by the inversion algorithm systematically give a proportion of ice water greater than 99 %, or a total content of dust always less than 5 ppmv (see Figure 12). This result tends to reinforce the hypothesis of a very effective cleaning of dust (Kieffer, 2007; Portyankina et al., 2010). On the contrary, water ice is not cleaned, or at least much less efficiently than dust because of a higher albedo. This behavior is expected, the dust being low albedo (around 0.3) compared to water ice, which may have a very high albedo, and the cleaning efficiency decreasing for a growing albedo (Portyankina et al., 2010). The graphs representing the total impurity content (fig. 11) can therefore be directly interpreted as a volumetric water content (with an error of less than 1 %).

In details, the two points studied in the dark spots show different behaviors: the DS1 point appears to have a level of contamination similar to that of the control points. Conversely, the DS2 point in the inter-dune appears to be considerably more contaminated with water ice than all other points studied, displaying impurity contents up to 5 times higher than other locations in early spring. The DS2 contamination then decreases in a few weeks to stabilize at the same level as the surrounding points.

The behavior of DS2 is consistent with the jet mechanism. Indeed, the triggering of a jet of gas is supposed to be a violent event, which tears material from the regolith and deposits it at the top of the layer of ice. It

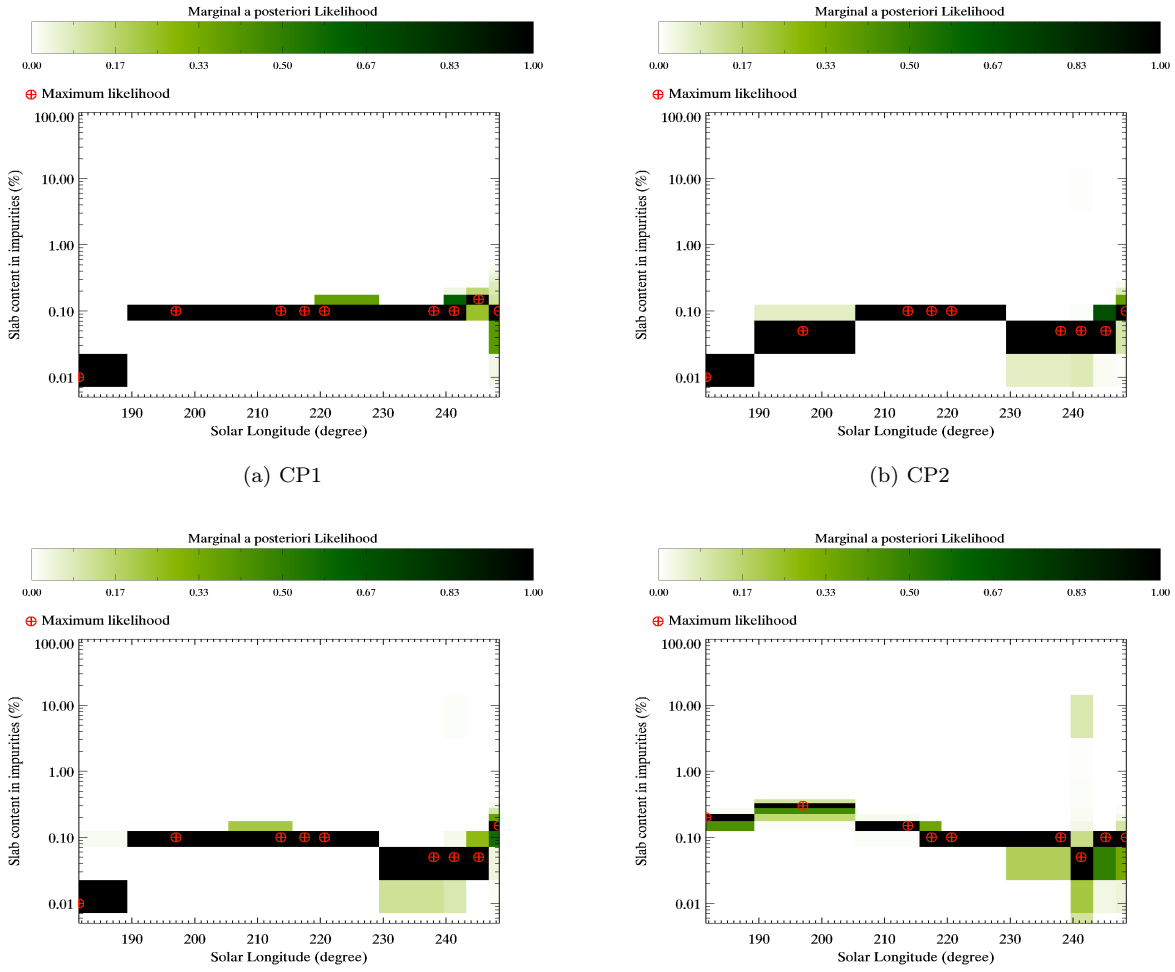


(a) CP1

(b) CP2

(c) DS1

(d) DS2

Figure 11: Evolution of the total content in impurities for (a) CP1 (b) CP2, (c) DS1 and (d) DS2. The shades of green and the red crosses are interpreted in the same way as in the figure 10.

is therefore expected that there will be more contamination in the vicinity of dark spots. Conversely, DS1's behavior is unexpected: its level of contamination is equivalent to that of the environmental control point. The apparent inconsistency with the jet mechanism can be resolved if most of the material ejected by the cold jet do not stay in the vicinity of the jet, but is either carried away by the wind, roll down the slope or is efficiently cleaned. It would also mean that the darkness of spot around the jet is a photometric effect. In addition, the upward sublimation flux of increasing intensity during spring favors a transport of dust and water ice grains down from the ridge of the dune to the inter-dunes, by decreasing the friction coefficient between the grains and the slope. This would explain the formation of flows from dark spots, such as the one in Fig. 4 from $L_S = 213^\circ$. In this case, it would be expected to find greater contamination in the inter-dune, or at least at the foot of the slopes. The follow-up of a control point precisely at the bottom of the slope would make it possible to decide on this point. Another possible explanation is that the jets in the inter-dunes contain much more water ice than the jets in the ridges: as the inter-dunes subsurface is most probably water ice rich (polygons) and the jet mechanism may pull water out from the subsurface to the fan (Kereszturi et al., 2011). It will later enrich the layer in water ice. Conversely, the dune is constituted of sand, and the jet will only pull dust, that will then be efficiently cleaned before the next measurement (Pommerol et al., 2011).

#### *4.4.2. Water grain size*

The figure 13 shows that the grain size increases during the spring for all the studied points, up to about $L_S = 238^\circ$ from 1 microns to 50 microns. Then grain size suddenly decreases up to few microns at the end of the season. Variations in water ice grain size are not expected during the sublimation of the seasonal $CO_2$ deposits. Indeed, water is supposed to be thermalized by $CO_2$ ice, as carbon dioxide has a condensation point much lower than water. So an evolution in the grain size means that water ice may have a significant mobility, even at the very beginning of the spring. This is unexpected and a mechanism able to explain the variations both in grain size and total content will be detailed in the following subsections.

#### *4.4.3. Water escape*

Water ice at the surface is in contact with $CO_2$ ice throughout the spring, which is a cold trap. Therefore $H_2O$ is not expected to sublimate as long as the ice of $CO_2$ has not completely disappeared. To remain the total water budget constant in a shrinking $CO_2$ slab, we expect an increase of volumetric water impurity. However, the combined analysis of the previous subsections clearly show that this is not the case. So there

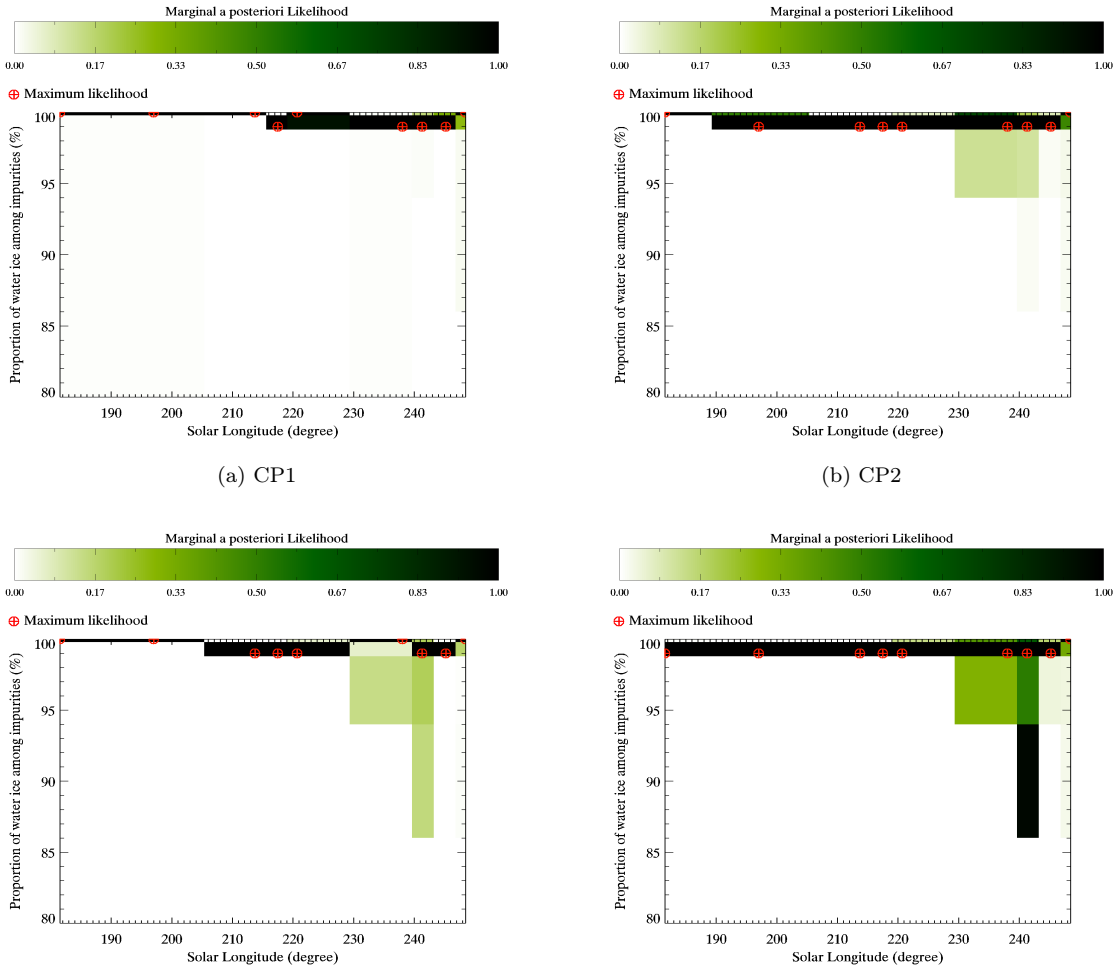


(a) CP1

(b) CP2

(c) DS1

(d) DS2

Figure 12: Evolution of the proportion of water ice among impurities (a) CP1 (b) CP2, (c) DS1 and (d) DS2. The shades of green and the red crosses are interpreted in the same way as in the figure 10.

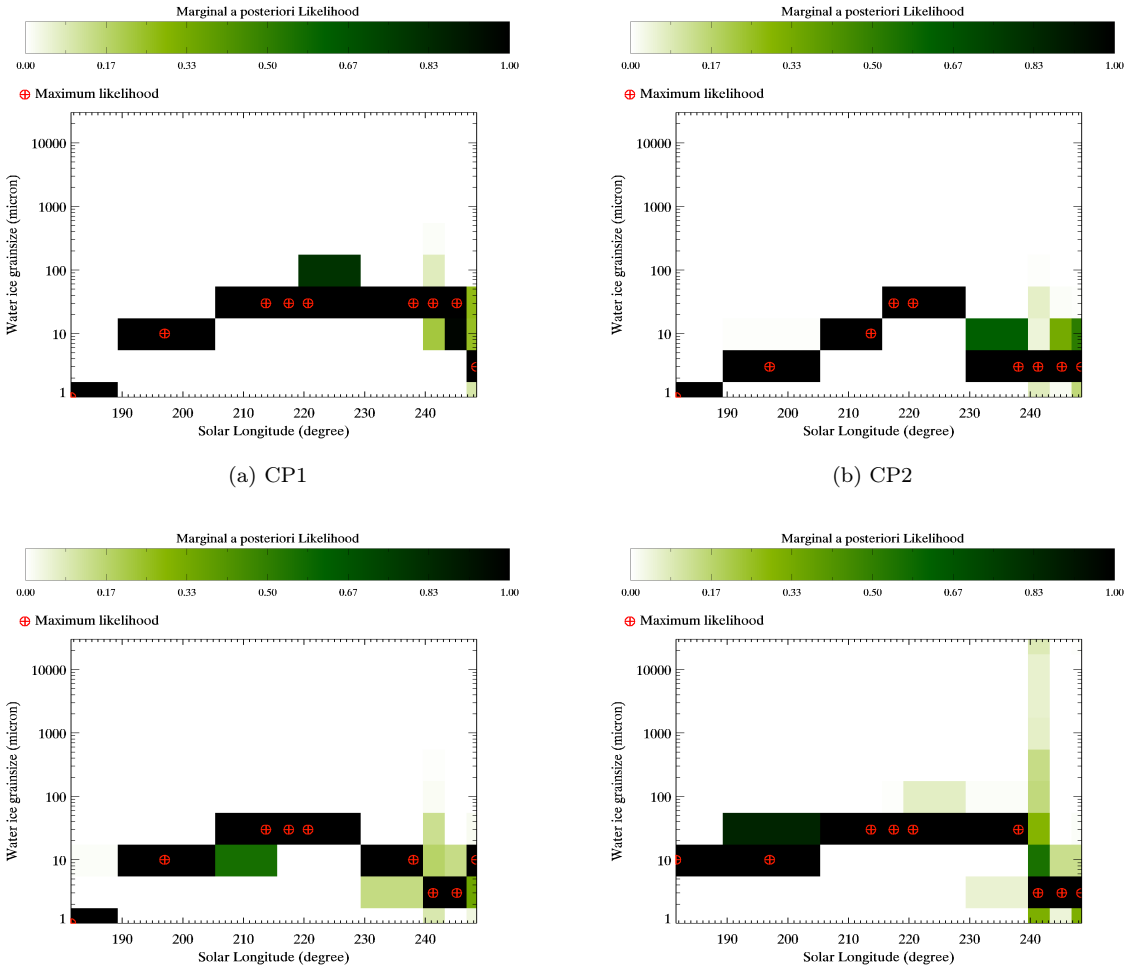


(a) CP1

(b) CP2

(c) DS1

(d) DS2

Figure 13: Evolution of the water ice grain diameter for (a) CP1 (b) CP2, (c) DS1 and (d) DS2. The shades of green and the red crosses are interpreted in the same way as in the figure 10.

is an water escape process. This escape can be explained by the spring activity of jets. Indeed, during an ejection, part of the water ice entrained by the jet can remain suspended in the atmosphere, carried by the ambient sublimation flux (Kieffer et al., 2000). In this case, the fine part of the water ice grains must gradually be eliminated over repeated ejections, and the grain size must therefore increase during the spring, as observed (fig. 13).

Note that water ice remain throughout spring present in amounts that are far lower than $CO_2$ (about 0.1%), and that there is no clear albedo variations such as those described by Pommerol et al., 2011. The formation of a thin water frost layer at the top of the subliming $CO_2$ ice layer would create an albedo increase that is not seen here. Therefore it is supposed that water ice is always in intimate mixing with $CO_2$ ice. Due to removal from the bottom and deposition at the top, there still may be a vertical variation of the water ice content inside the $CO_2$ ice layer, that is not taken into account in the inversion. All quantities are vertically averaged.

#### *4.4.4. Dust in linear mix*

The jet mechanism proposed to explain dark spots involves the deposition of a layer of dust and possibly water ice at the top of the layer after ejection. If the layer is thick enough locally, one should observe, either only dust in the center of the dark spot, or a linear mixture between two types of surface: dust and ice. We can see in Fig. 14 that there is no significant difference in terms of sub-pixel geographic mixing of dust and ice between points. Moreover, it can be noted that all the points studied exhibit a similar behavior, with a small peak of contamination around $L_S = 220°$ that can be explained by a possible dust storm, as also see in the atmospheric dust content estimate (see table 3). Then, the surface proportion of dust increase from $L_S = 238°$ to the end. This is probably due to the fact that from this date the $CO_2$ has been totally sublimated on some areas of the image. This explanation is consistent with the sudden decrease in grain size observed in fig. 13. Indeed, $CO_2$ ice forces the temperature of the media in contact with it to its equilibrium temperature (about 150 K), but when the $CO_2$ has disappeared, dust and water ice are no longer buffered by this $CO_2$ condensation temperature. In this case, the temperature increases, and the water ice finally sublimates. However, there are still ice-covered areas of $CO_2$ a few meters away, and water could be trapped again. Water re condensed at the surface, forming a fine frost, explaining the sudden decrease in the size of the observed grains. This mechanism was also observed in the north, the sublimation of seasonal deposits leading to the formation of a ring of water frost following the recession of the seasonal cap (Wagstaff et al., 2008; Appéré et al., 2011; Appéré, 2012; Pommerol et al., 2013).

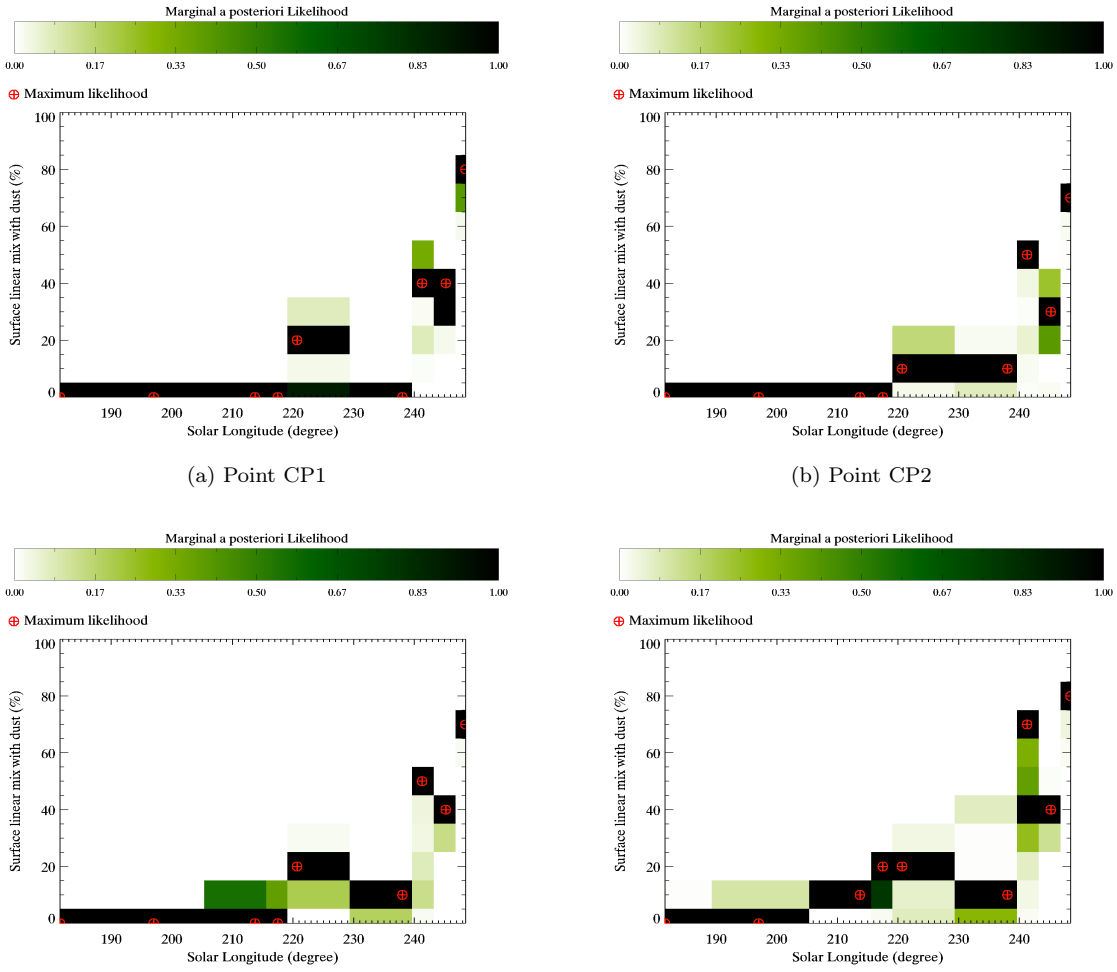


(a) Point CP1

(b) Point CP2

(c) Point DS1

(d) Point DS2

Figure 14: Evolution of the proportion of dust in linear mix for (a) CP1 (b) CP2, (c) DS1 and (d) DS2. The shades of green and the red crosses are interpreted in the same way as in the figure 10.

It is worth to remind that, on the wavelength range $1\,\mu$ m $- 2.6\,\mu$ m, the pure dust has a spectral behavior very monotonic, quasi-linear. In fact, it is difficult to distinguish the effects of aerosols in the atmosphere from dust within the ice layer. It is therefore expected to have high uncertainty on dust contamination estimates by the inversion algorithm. Actually, this is not the case in our results: the amounts of dust are very well constrained, even tacking into account the uncertainties due to atmospheric correction. We attribute this behavior to the non-linear coupling between $CO_2$ bands and dust within the slab. The same behavior may also occur in case of differentiation between linear surface mixing with non-linear impurities. Again our results show that there is enough information in the spectral data to decipher this situation, most probably due to the non-linearities.

It would still be interesting to test the algorithm with other atmospheric correction methods. For example, the photometric properties of aerosols can be used to better isolate them and improve the correction (Douté et al., 2013; Douté, 2014).

## 5. Discussion

We propose a sketch (see fig. 15) to summarize the evolution of the seasonal cap in Richardson crater in dark spots and off dark spots.

*Mechanism for water escape.* We propose a mechanism of escape of water ice, which would be incorporated into the atmosphere, from $L_S = 190°$, in a way consistent with the jet mechanism proposed by Piqueux et al., 2003 and Kieffer et al., 2006; Kieffer, 2007.

If we consider that the sublimation flux can raise grains of dust of a supposed density of 2200 kg.m$^{-3}$ up to a radius of 3.5$\mu$m (Kieffer et al., 2000; Kieffer, 2007), it is clear that water ice grains with a density of about 920 kg.m$^{-3}$ may be suspended to larger radii up to 10 microns. Step by step, all the grains smaller than this radius will be eliminated (see Figure 15 d and e). Before the abrupt decrease $L_s = 240°$, the grain size seems to stabilize around a value between $10\,\mu$m and $30\,\mu$m (see fig. 13). This value is consistent with the grain sizes that can escape.

OMEGA observations suggest an enrichment of the atmosphere at these latitudes from $L_S = 250°$ (Melchiorri et al., 2009), and are not incompatible with an enrichment earlier in the season. It would be interesting to study these observations of atmospheric water vapor in more detail.

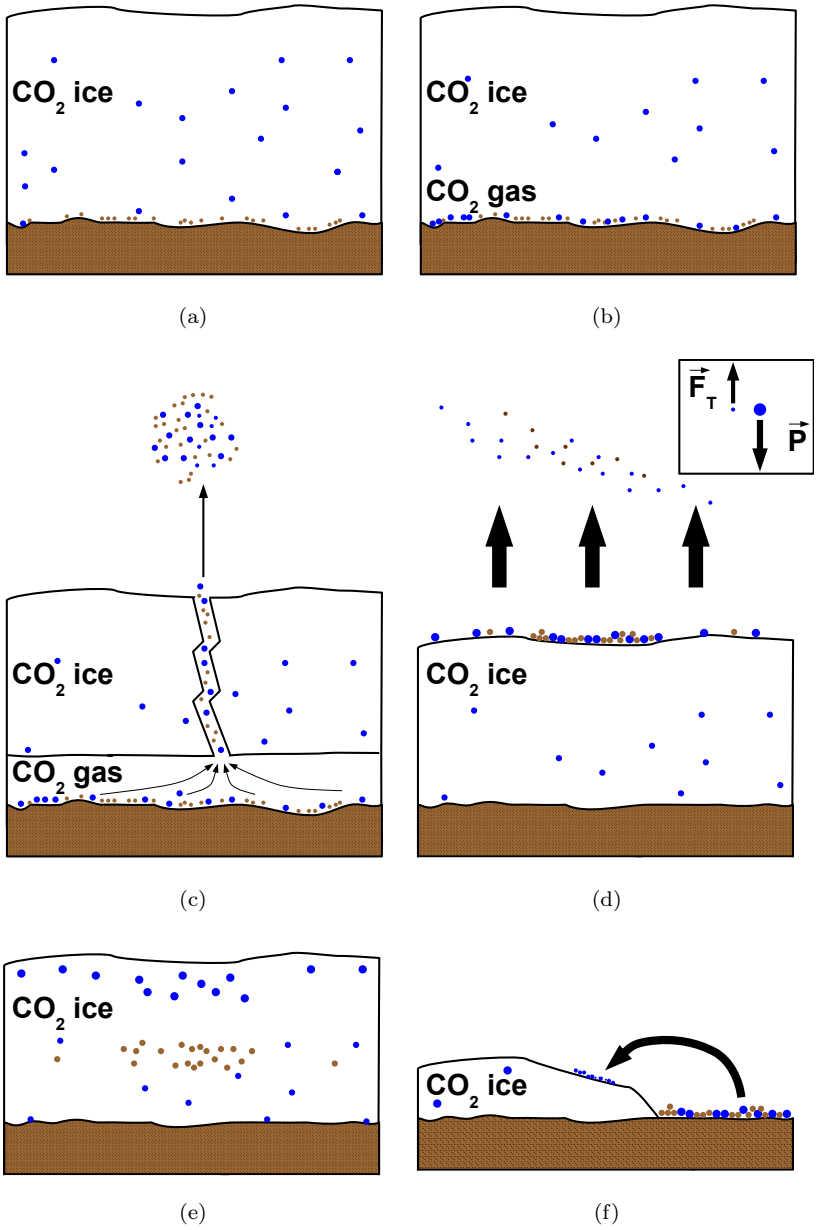


Figure 15: Proposed model for the evolution of seasonal ice deposits during spring. (a) At the beginning of the spring the ice layer becomes compact in slab form ($L_S \sim 181°$), In the meantime, it is cleaned of the impurities of dust and ice thanks to solar irradiation (b) Basal ice sublimation starts, and the impurities that were trapped in the ice are accumulated at the bottom of the layer. This is the first stage of the cold geyser model. (c) The pressure built inside pockets under the layer reaches the ice breaking threshold. The ice breaks and gas escapes brutally, carrying impurities with it. (d) Small grains are lifted and put into suspension into the atmosphere, while large one fall back to the ground. Small water ice grains that are put into suspension will eventually sublimate and be integrated to the global water circulation. Dust is deposited in a superficial layer. (e) In the place of a cold jet, the deposited layer of dust and water ice is sinking. The dust sink very rapidly, and the water ice is integrated to the layer due to the condensation of $CO_2$ at night at the top of the layer, and the sublimation during the day of de $CO_2$ ice at the bottom of the layer. (f) If a patch of terrain is completely defrosted, then the ground is no more thermally buffered to the equilibrium temperature of $CO_2$ ice. The temperature rises and the water ice sublimates. If $CO_2$ ice is still present in the area, it will act as a cold trap, and the just sublimated water will condense on the closest patch of $CO_2$ ice.

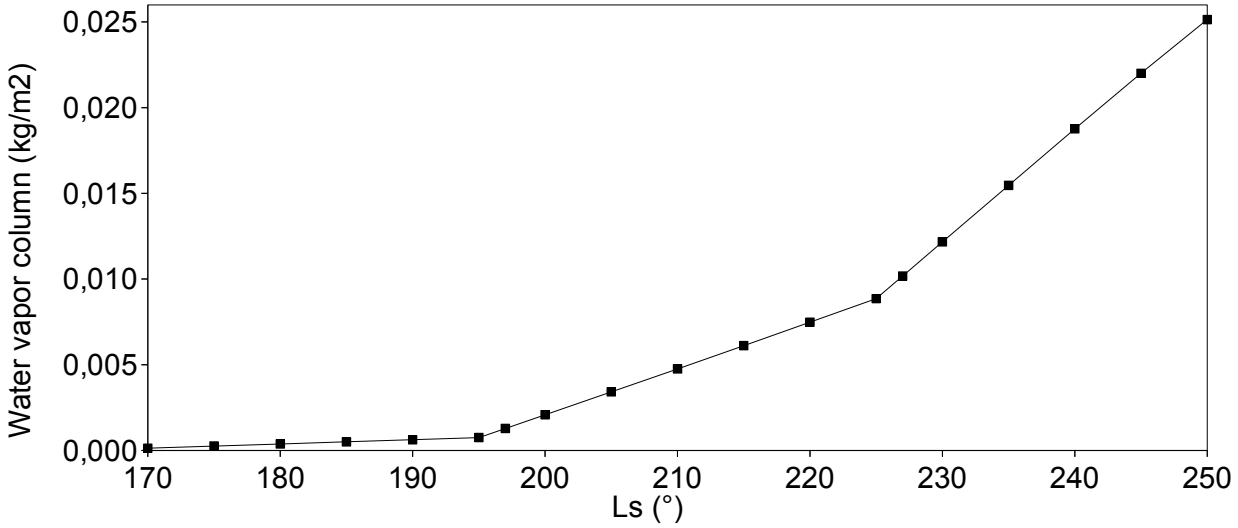


Figure 16: Atmospheric water vapor content in the studied area, predicted by a GCM (Millour et al., 2014 ©LMD/OU/IAA/ESA/CNES).

The water escape noted in section 4.4.1 is also consistent with an enrichment of atmospheric vapor during the spring predicted by climatic models (Forget et al., 2006; Millour et al., 2014), as we can see it in figure 16. This enrichment is becoming more and more important as the season advances. This increase in the quantity of water vapor predicted in the atmosphere by the GCMs can be linked, on one hand, to the increase in atmospheric pressure and, on the other hand, to forcing.

*Rolling layer mechanism.* According to MCD (Forget et al., 1999; Forget et al., 2006; Millour et al., 2014), at the latitude of Richardson crater, 1.5 kg of $CO_2$ ice recondenses each night per square meter at the beginning of the spring. We can assume that this ice condenses mostly at the top of the layer (Pilorget et al., 2011) (because of the opacity of the $CO_2$ to thermal radiations, and because condensation is exothermic). This means that from Ls=170° to Ls=250°, from the beginning tho the end of the sublimation of the seasonal deposit, a total amount of 112 kg of $CO_2$ ice recondenses per square meter meaning up to 70 mm of $CO_2$ ice recondenses at the surface. To determine this amount, we simply consider that the amount of recondensed $CO_2$ decreases linearly to 0 at LS=250°. This represents more than 15% of the initial thickness of the layer. This lead us to assume that the large water ice grains that are ejected during a cold jet event, are re-integrated to the slab layer (see figure15e) by the condensation of $CO_2$ above them at night.

## 6. Conclusions and perspectives

The main results provided by our data analysis are: (i) $CO_2$ ice is most probably in a translucent state during the whole spring, instead of a granular one, as previously thought. (ii) Retrieved seasonal variations of translucent ice thickness is consistent with GCM prediction. (iii) Only few ppmv of dust are present in the $CO_2$ ice slab during the spring. (iv) Since the water ice content is 0.1%v throughout the spring season but the $CO_2$ ice is shrinking, we must conclude that a water escape occurs. The escape of water into the atmosphere seems to be in agreement with water vapor measurements. (v) The water grain size increases during the spring from 1 to 50 microns and suddenly falls down again.

Using all these new constraints, we propose a new sketch to explain the microphysics of the seasonal south polar cap. We propose a refined cryoventing mechanism in the presence of water ice: the water ice accumulates at the bottom of the layer as a result of the slab sublimation from the bottom. Then water ice grains are ejected during cryoventing episodes. The larger grains fall back on the layer, while the smaller ones are lifted by the general sublimation flux, and integrated to the atmospheric circulation. In the last stage, the water from already defrosted regions condenses onto $CO_2$ ice that acts as a cold-trap.

The small grain size of water that are incorporated into the general circulation, should most probably sublimate. Future work, using for instance limb measurements of MCS data, should confirm this mechanism. Also the effect of this mechanism to the general circulation should be studied by numerical simulations. Other study using CRISM data in other location of the south pole, or even the north pole would be interesting in order to determine if the proposed sketch is general on Mars or particular to the Richardson crater. In this perspective, regional scale analysis using OMEGA and the large footprint mode of CRISM should also be conducted.

*Acknowledgement*

We acknowledge support from the “Institut National des Sciences de l’Univers” (INSU), the "Centre National de la Recherche Scientifique" (CNRS) and "Centre National d’Etude Spatiale" (CNES) and through the "Programme National de Planétologie" and MEX/OMEGA Program. The project « Multiplaneto » has been granted in 2015 and 2016 by Défi Imag’In/CNRS.

**References**


Andrieu, F., Douté, S., Schmidt, F., Schmitt, B., Nov 2015. Radiative transfer model for contaminated rough slabs. Appl. Opt. 54 (31), 9228–9241.
URL http://ao.osa.org/abstract.cfm?URI=ao-54-31-9228

Andrieu, F., Schmidt, F., Douté, S., 2014. $CO_2$ ice composition and evolution on Mars: A radiative transfer inversion. In: Lunar and Planetary Science Conference. Vol. 45. p. 1148.

Andrieu, F., Schmidt, F., Schmitt, B., Douté, S., Brissaud, O., 2016. Retrieving the characteristics of slab ice covering snow by remote sensing. The Cryosphere 10 (5), 2113–2128.
URL http://www.the-cryosphere.net/10/2113/2016/

Appéré, T., 2012. Cycle actuel de l'eau sur Mars: étude des dépôts saisonniers de l'hémisphère nord par télédétection hyperspectrale (OMEGA/Mars Express). Ph.D. thesis, Université de Grenoble.

Appéré, T., Schmitt, B., Langevin, Y., Douté, S., Pommerol, A., Forget, F., Spiga, A., Gondet, B., Bibring, J.-P., 2011. Winter and spring evolution of northern seasonal deposits on Mars from OMEGA on Mars Express. J. Geophys. Res., 116, E05001
URL http://dx.doi.org/10.1029/2010JE003762

Ceamanos, X., Douté, S., Fernando, J., Schmidt, F., Pinet, P., Lyapustin, A., 2013. Surface reflectance of Mars observed by CRISM/MRO: 1. multi-angle approach for retrieval of surface reflectance from CRISM observations (mars-reco). Journal of Geophysical Research: Planets 118 (3), 514–533.
URL http://dx.doi.org/10.1029/2012JE004195

Douté, S., Jun. 2014. Monitoring atmospheric dust spring activity at high southern latitudes on Mars using OMEGA. Planetary and Space Science 96 (0), 1–21.
URL http://www.sciencedirect.com/science/article/pii/S003206331400004X

Douté, S., Ceamanos, X., Appéré, T., Sep. 2013. Retrieving atmospheric dust opacity on Mars by imaging spectroscopy at large angles. Planetary and Space Science 85, 38–52.
URL http://www.sciencedirect.com/science/article/pii/S0032063313001347

Douté, S., Schmitt, B., 1998. A multilayer bidirectional reflectance model for the analysis of planetary surface hyperspectral images at visible and near-infrared wavelengths. J. Geophys. Res. 103 (E13), 31367–31389.
URL http://dx.doi.org/10.1029/98JE01894

Douté, S., Schmitt, B., Langevin, Y., Bibring, J.-P., Altieri, F., Bellucci, G., Gondet, B., Poulet, F., Jan. 2007. South pole of Mars: nature and composition of the icy terrains from Mars Express OMEGA observations. Planetary and Space Science 55 (1-2), 113–133.
URL http://www.sciencedirect.com/science/article/pii/S0032063306001243

Edgett, K. S., Supulver, K. D., Malin, M. C., Aug. 2000. Spring Defrosting of Martian Polar Regions: Mars Global Surveyor MOC and TES Monitoring of the Richardson Crater Dune Field, 1999-2000. In: Second International Conference on Mars Polar Science and Exploration. p. 34.

Fernando, J., Schmidt, F., Ceamanos, X., Pinet, P., Douté, S., Daydou, Y., 2013. Surface reflectance of Mars observed by CRISM/MRO: 2. estimation of surface photometric properties in Gusev crater and Meridiani planum. Journal of Geophysical Research: Planets 118 (3), 534–559.
URL http://dx.doi.org/10.1029/2012JE004194

Fernando, J., Schmidt, F., Pilorget, C., Pinet, P., Ceamanos, X., Douté, S., Daydou, Y., Costard, F., Jun. 2015. Characterization and mapping of surface physical properties of Mars from CRISM multi-angular data: Application to Gusev crater and Meridiani planum. Icarus 253, 271–295.
URL http://www.sciencedirect.com/science/article/pii/S0019103515001128

Forget, F., Hourdin, F., Fournier, R., Hourdin, C., Talagrand, O., Collins, M., Lewis, S. R., Read, P. L., Huot, J.-P., 1999. Improved general circulation models of the Martian atmosphere from the surface to above 80 km. Journal of Geophysical Research: Planets 104 (E10), 24155–24175.
URL http://dx.doi.org/10.1029/1999JE001025

Forget, F., Millour, E., Lebonnois, S., Montabone, L., Dassas, K., Lewis, S. R., Read, P. L., López-Valverde, M. A., González-Galindo, F., Montmessin, F., Lefèvre, F., Desjean, M.-C., Huot, J.-P., Feb. 2006. The new Mars climate database. In: Forget, F., Lopez-Valverde, M. A., Desjean, M. C., Huot, J. P., Lefevre, F., Lebonnois, S., Lewis, S. R., Millour, E., Read, P. L., Wilson, R. J. (Eds.), Mars Atmosphere Modelling and Observations. p. 128.

Forward, K. M., Lacks, D. J., Sankaran, R. M., 2009. Particle-size dependent bipolar charging of Martian regolith simulant. Geophysical Research Letters 36, L13201.
URL http://dx.doi.org/10.1029/2009GL038589

Hansen, C., Byrne, S., Portyankina, G., Bourke, M., Dundas, C., McEwen, A., Mellon, M., Pommerol, A., Thomas, N., 2013. Observations of the northern seasonal polar cap on Mars: I. spring sublimation activity and processes. Icarus 225 (2), 881 – 897, Mars Polar Science V.
URL http://www.sciencedirect.com/science/article/pii/S0019103512003971

Hansen, C., Thomas, N., Portyankina, G., McEwen, A., Becker, T., Byrne, S., Herkenhoff, K., Kieffer, H., Mellon, M., Jan. 2010. HiRISE observations of gas sublimation-driven activity in Mars' southern polar regions: I. erosion of the surface. Icarus 205 (1), 283–295.
URL http://www.sciencedirect.com/science/article/pii/S0019103509003133

Hapke, B., Jul. 1984. Bidirectional reflectance spectroscopy: 3. correction for macroscopic roughness. Icarus 59 (1), 41–59.
URL http://www.sciencedirect.com/science/article/pii/001910358490054X

Hapke, B., 2012. Theory of Reflectance and Emittance Spectroscopy. Cambridge University Press.

Kereszturi, A., Vincendon, M., Schmidt, F., Jan. 2011. Water ice in the dark dune spots of Richardson crater on Mars. Planetary and Space Science 59 (1), 26–42.
URL http://www.sciencedirect.com/science/article/pii/S0032063310003235

Kieffer, H. H., 2007. Cold jets in the Martian polar caps. Journal of Geophysical Research: Planets (1991–2012) 112 (E8).

Kieffer, H. H., Christensen, P. R., Titus, T. N., Aug. 2006. $CO_2$ jets formed by sublimation beneath translucent slab ice in Mars' seasonal south polar ice cap. Nature 442 (7104), 793–796.
URL http://dx.doi.org/10.1038/nature04945

Kieffer, H. H., Titus, T. N., Mullins, K. F., Christensen, P. R., 2000. Mars south polar spring and summer behavior observed by TES: Seasonal cap evolution controlled by frost grain size. Journal of Geophysical Research: Planets 105 (E4), 9653–9699.
URL http://dx.doi.org/10.1029/1999JE001136

Langevin, Y., Bibring, J.-P., Montmessin, F., Forget, F., Vincendon, M., Douté, S., Poulet, F., Gondet, B., Jul. 2007. Observations of the south seasonal cap of Mars during recession in 2004 8211;2006 by the OMEGA visible/near-infrared imaging spectrometer on board Mars Express. J. Geophys. Res. 112 (E8), E08S12–.
URL http://dx.doi.org/10.1029/2006JE002841

Leighton, R. B., Murray, B. C., Jul. 1966. Behavior of carbon dioxide and other volatiles on Mars. Science 153 (3732), 136–144.
URL http://www.sciencemag.org/content/153/3732/136.abstract

Lewis, S. R., Collins, M., Read, P. L., Forget, F., Hourdin, F., Fournier, R., Hourdin, C., Talagrand, O., Huot, J.-P., 1999. A climate database for Mars. Journal of Geophysical Research: Planets 104 (E10),

24177–24194.

URL http://dx.doi.org/10.1029/1999JE001024

Mahaffy, P. R., Webster, C. R., Atreya, S. K., Franz, H., Wong, M., Conrad, P. G., Harpold, D., Jones, J. J., Leshin, L. A., Manning, H., Owen, T., Pepin, R. O., Squyres, S., Trainer, M., Team, M. S., 2013. Abundance and isotopic composition of gases in the Martian atmosphere from the Curiosity rover. Science 341 (6143), 263–266.

URL http://www.sciencemag.org/content/341/6143/263.abstract

Martinez, G., Renno, N., Elliott, H., 2012. The evolution of the albedo of dark spots observed on Mars polar region. Icarus 221 (2), 816 – 830.

URL http://www.sciencedirect.com/science/article/pii/S0019103512003697

McEwen, A. S., Eliason, E. M., Bergstrom, J. W., Bridges, N. T., Hansen, C. J., Delamere, W. A., Grant, J. A., Gulick, V. C., Herkenhoff, K. E., Keszthelyi, L., Kirk, R. L., Mellon, M. T., Squyres, S. W., Thomas, N., Weitz, C. M., May 2007. Mars Reconnaissance Orbiter's High Resolution Imaging Science Experiment (HiRISE). J. Geophys. Res. 112 (E5), E05S02–.

URL http://dx.doi.org/10.1029/2005JE002605

Melchiorri, R., Encrenaz, T., Drossart, P., Fouchet, T., Forget, F., Titov, D., Maltagliati, L., Altieri, F., Vincendon, M., Langevin, Y., Bibring, J., May 2009. OMEGA/Mars Express: South pole region, water vapor daily variability. Icarus 201 (1), 102–112.

URL http://www.sciencedirect.com/science/article/pii/S0019103508004466

Millour, E., Forget, F., Lefevre, F., Gonzalez-Galindo, F., Lopez-Valverde, M., Montabone, L., Colaitis, A., Navarro, T., Chauffray, J.-Y., Jul. 2012. The latest improvements in the LMD Global Climate Model and derived Mars Climate Database (version 5). In: 39th COSPAR Scientific Assembly. Vol. 39 of COSPAR Meeting. p. 1239.

Millour, E., Forget, F., Spiga, A., Navarro, T., Madeleine, J.-B., Pottier, A., Montabone, L., Kerber, L., Lefèvre, F., Montmessin, F., et al., 2014. The latest Mars Climate Database (MCD v5. 1). In: EGU General Assembly Conference Abstracts. Vol. 16. p. 2102.

Mischna, M. A., Richardson, M. I., Wilson, R. J., McCleese, D. J., 2003. On the orbital forcing of Martian water and $CO_2$ cycles: A general circulation model study with simplified volatile schemes. Journal of Geophysical Research: Planets 108 (E6), n/a–n/a, 5062.

URL http://dx.doi.org/10.1029/2003JE002051

Mohlmann, D., Kereszturi, A., Jun. 2010. Viscous liquid film flow on dune slopes of Mars. Icarus 207 (2), 654–658.
URL http://www.sciencedirect.com/science/article/pii/S0019103510000047

Murchie, S., Arvidson, R., Bedini, P., Beisser, K., Bibring, J.-P., Bishop, J., Boldt, J., Cavender, P., Choo, T., Clancy, R. T., Darlington, E. H., Des Marais, D., Espiritu, R., Fort, D., Green, R., Guinness, E., Hayes, J., Hash, C., Heffernan, K., Hemmler, J., Heyler, G., Humm, D., Hutcheson, J., Izenberg, N., Lee, R., Lees, J., Lohr, D., Malaret, E., Martin, T., McGovern, J. A., McGuire, P., Morris, R., Mustard, J., Pelkey, S., Rhodes, E., Robinson, M., Roush, T., Schaefer, E., Seagrave, G., Seelos, F., Silverglate, P., Slavney, S., Smith, M., Shyong, W.-J., Strohbehn, K., Taylor, H., Thompson, P., Tossman, B., Wirzburger, M., Wolff, M., May 2007. Compact Reconnaissance Imaging Spectrometer for Mars (CRISM) on Mars Reconnaissance Orbiter (MRO). J. Geophys. Res. 112 (E5), E05S03–.
URL http://dx.doi.org/10.1029/2006JE002682

Owen, T., Biemann, K., Rushneck, D. R., Biller, J. E., Howarth, D. W., Lafleur, A. L., 1977. The composition of the atmosphere at the surface of Mars. Journal of Geophysical Research 82 (28), 4635–4639.
URL http://dx.doi.org/10.1029/JS082i028p04635

Pilorget, C., Forget, F., Millour, E., Vincendon, M., Madeleine, J., May 2011. Dark spots and cold jets in the polar regions of Mars: New clues from a thermal model of surface $CO_2$ ice. Icarus 213 (1), 131–149.
URL http://www.sciencedirect.com/science/article/pii/S001910351100042X

Piqueux, S., Byrne, S., Richardson, M. I., Aug. 2003. Sublimation of Mars's southern seasonal $CO_2$ ice cap and the formation of spiders. J. Geophys. Res. 108 (E8), 5084–.
URL http://dx.doi.org/10.1029/2002JE002007

Pommerol, A., Appéré, T., Portyankina, G., Aye, K.-M., Thomas, N., Hansen, C., 2013. Observations of the northern seasonal polar cap on Mars III: CRISM/HiRISE observations of spring sublimation. Icarus 225 (2), 911 – 922, Mars Polar Science V.
URL http://www.sciencedirect.com/science/article/pii/S0019103512003582

Pommerol, A., Portyankina, G., Thomas, N., Aye, K.-M., Hansen, C. J., Vincendon, M., Langevin, Y., Aug. 2011. Evolution of south seasonal cap during Martian spring: Insights from high-resolution observations by HiRISE and CRISM on mars reconnaissance orbiter. J. Geophys. Res. 116 (E8), E08007–.
URL http://dx.doi.org/10.1029/2010JE003790

Portyankina, G., Markiewicz, W. J., Thomas, N., Hansen, C. J., Milazzo, M., Jan. 2010. HiRISE observations of gas sublimation-driven activity in Mars' southern polar regions: III. models of processes involving

translucent ice. Icarus 205 (1), 311–320.
URL http://www.sciencedirect.com/science/article/pii/S0019103509003893

Schmidt, F., Fernando, J., Nov. 2015. Realistic uncertainties on Hapke model parameters from photometric measurement. Icarus 260, 73–93.
URL http://www.sciencedirect.com/science/article/pii/S0019103515002936

Schmitt, B., Quirico, E., Trotta, F., Grundy, W. M., 1998. Optical properties of ices from UV to infrared. In: Schmitt, B., de Bergh, C., Festou, M. (Eds.), Solar System Ices. Vol. 227 of Astrophysics and Space Science Library. Kluwer, pp. 199–240.

Shkuratov, Y., Starukhina, L., Hoffmann, H., Arnold, G., Feb. 1999. A model of spectral albedo of particulate surfaces: Implications for optical properties of the Moon. Icarus 137 (2), 235–246.
URL http://www.sciencedirect.com/science/article/pii/S0019103598960353

Singh, D., Flanner, M., 2016. An improved carbon dioxide snow spectral albedo model: Application to Martian conditions. Journal of Geophysical Research: Planets 121 (10), 2037–2054.

Smith, M. D., Aug. 2009. THEMIS observations of Mars aerosol optical depth from 2002-2008. Icarus 202 (2), 444–452.
URL http://www.sciencedirect.com/science/article/pii/S0019103509001365

Supulver, K. D., Edgett, K. S., Malin, M. C., Mar. 2001. Seasonal Changes in Frost Cover in the Martian South Polar Region: Mars Global Surveyor MOC and TES Monitoring of the Richardson Crater Dune Field. In: Lunar and Planetary Science Conference. Vol. 32 of Lunar and Planetary Science Conference. p. 1966.

Thomas, N., Portyankina, G., Hansen, C., Pommerol, A., Mar. 2011. HiRISE observations of gas sublimation-driven activity in Mars southern polar regions: IV. fluid dynamics models of $CO_2$ jets. Icarus 212 (1), 66–85.
URL http://www.sciencedirect.com/science/article/pii/S0019103510004847

Tillman, J. E., 1988. Mars global atmospheric oscillations: Annually synchronized, transient normal-mode oscillations and the triggering of global dust storms. Journal of Geophysical Research: Atmospheres 93 (D8), 9433–9451.
URL http://dx.doi.org/10.1029/JD093iD08p09433

Vincendon, M., Feb. 2013. Mars surface phase function constrained by orbital observations. Planetary and Space Science 76, 87–95.
URL http://www.sciencedirect.com/science/article/pii/S0032063312003820

Vincendon, M., Langevin, Y., Poulet, F., Bibring, J.-P., Gondet, B., 2007. Recovery of surface reflectance spectra and evaluation of the optical depth of aerosols in the near-ir using a monte carlo approach: Application to the OMEGA observations of high-latitude regions of Mars. Journal of Geophysical Research: Planets 112 (E8), n/a–n/a, e08S13.
URL http://dx.doi.org/10.1029/2006JE002845

Vincendon, M., Langevin, Y., Poulet, F., Bibring, J.-P., Gondet, B., Jouglet, D., Aug. 2008. Dust aerosols above the south polar cap of Mars as seen by OMEGA. Icarus 196 (2), 488–505.
URL http://www.sciencedirect.com/science/article/pii/S0019103507006082

Vincendon, M., Langevin, Y., Poulet, F., Pommerol, A., Wolff, M., Bibring, J.-P., Gondet, B., Jouglet, D., Apr. 2009. Yearly and seasonal variations of low albedo surfaces on Mars in the OMEGA/MEX dataset: Constraints on aerosols properties and dust deposits. Icarus 200 (2), 395–405.
URL http://www.sciencedirect.com/science/article/pii/S0019103508004387

Wagstaff, K. L., Titus, T. N., Ivanov, A. B., Castano, R., Bandfield, J. L., Feb. 2008. Observations of the north polar water ice annulus on Mars using THEMIS and TES. Planetary and Space Science 56 (2), 256–265.
URL http://www.sciencedirect.com/science/article/pii/S0032063307002103

Wolff, M. J., Smith, M. D., Clancy, R. T., Arvidson, R., Kahre, M., Seelos, F., I., Murchie, S., Savijarvi, H., Jun. 2009. Wavelength dependence of dust aerosol single scattering albedo as observed by the Compact Reconnaissance Imaging Spectrometer. J. Geophys. Res. 114, E00D04–.
URL http://dx.doi.org/10.1029/2009JE003350